

REPORT DOCUMENTATION PAGE			Form Approved OMB NO. 0704-0188		
<p>The public reporting burden for this collection of information is estimated to average 1 hour per response, including the time for reviewing instructions, searching existing data sources, gathering and maintaining the data needed, and completing and reviewing the collection of information. Send comments regarding this burden estimate or any other aspect of this collection of information, including suggestions for reducing this burden, to Washington Headquarters Services, Directorate for Information Operations and Reports, 1215 Jefferson Davis Highway, Suite 1204, Arlington VA, 22202-4302. Respondents should be aware that notwithstanding any other provision of law, no person shall be subject to any penalty for failing to comply with a collection of information if it does not display a currently valid OMB control number.</p> <p>PLEASE DO NOT RETURN YOUR FORM TO THE ABOVE ADDRESS.</p>					
1. REPORT DATE (DD-MM-YYYY) 30-05-2014		2. REPORT TYPE Final Report		3. DATES COVERED (From - To) 1-Oct-2009 - 31-Mar-2014	
4. TITLE AND SUBTITLE Membrane Reflector Vertical Cavity Lasers at Near- and Midwave-Infrared			5a. CONTRACT NUMBER W911NF-09-1-0505		
			5b. GRANT NUMBER		
			5c. PROGRAM ELEMENT NUMBER 611102		
6. AUTHORS Weidong Zhou, Zhenqiang Ma			5d. PROJECT NUMBER		
			5e. TASK NUMBER		
			5f. WORK UNIT NUMBER		
7. PERFORMING ORGANIZATION NAMES AND ADDRESSES University of Texas at Arlington Grant and Contract Services 701 S. Nedderman Drive, Box 19145 Arlington, TX 76019 -0145			8. PERFORMING ORGANIZATION REPORT NUMBER		
9. SPONSORING/MONITORING AGENCY NAME(S) AND ADDRESS (ES) U.S. Army Research Office P.O. Box 12211 Research Triangle Park, NC 27709-2211			10. SPONSOR/MONITOR'S ACRONYM(S) ARO		
			11. SPONSOR/MONITOR'S REPORT NUMBER(S) 56099-EL.29		
12. DISTRIBUTION AVAILABILITY STATEMENT Approved for Public Release; Distribution Unlimited					
13. SUPPLEMENTARY NOTES The views, opinions and/or findings contained in this report are those of the author(s) and should not be construed as an official Department of the Army position, policy or decision, unless so designated by other documentation.					
14. ABSTRACT We carried out both fundamental and developmental research on a novel DBR-free membrane reflector based VCSELs (MR-VCSELs), with the demonstration of 1550 nm lasing operation at room temperature. The laser consists of an InGaAsP QW based heterostructure, sandwiched in between two single-layer photonic crystal Fano resonance silicon nanomembrane reflectors. Detailed theoretical and experimental work has been carried out towards high performance single layer broadband membrane reflector demonstrations, MR-VCSEL cavity design, and optically pumped laser demonstration at room temperature. The thermally engineering membrane reflectors					
15. SUBJECT TERMS Infrared lasers, VCSELs, silicon photonics, photonic crystals, nanomembrane, transfer printing					
16. SECURITY CLASSIFICATION OF:			17. LIMITATION OF ABSTRACT UU	15. NUMBER OF PAGES	19a. NAME OF RESPONSIBLE PERSON Weidong Zhou
a. REPORT UU	b. ABSTRACT UU	c. THIS PAGE UU			19b. TELEPHONE NUMBER 817-272-1227

## **Report Title**

### **Membrane Reflector Vertical Cavity Lasers at Near- and Midwave-Infrared**

#### **ABSTRACT**

We carried out both fundamental and developmental research on a novel DBR-free membrane reflector based VCSELs (MR-VCSELs), with the demonstration of 1550 nm lasing operation at room temperature. The laser consists of an InGaAsP QW based heterostructure, sandwiched in between two single-layer photonic crystal Fano resonance silicon nanomembrane reflectors. Detailed theoretical and experimental work has been carried out towards high performance single layer broadband membrane reflector demonstrations, MR-VCSEL cavity design, and optically pumped laser demonstration at room temperature. The thermally engineering membrane reflectors have also been investigated for high performance lasers.

**Enter List of papers submitted or published that acknowledge ARO support from the start of the project to the date of this printing. List the papers, including journal references, in the following categories:**

**(a) Papers published in peer-reviewed journals (N/A for none)**

<u>Received</u>	<u>Paper</u>
05/30/2014 20.00	Weidong Zhou, Deyin Zhao, Zhenqiang Ma. Field penetrations in photonic crystal Fano reflectors, Optics Express, (06 2010): 0. doi: 10.1364/OE.18.014152
05/30/2014 28.00	Weidong Zhou, Deyin Zhao, Yi-Chen Shuai, Hongjun Yang, Santhad Chuwongin, Arvinder Chadha, Jung-Hun Seo, Ken X. Wang, Victor Liu, Zhenqiang Ma, Shanhui Fan. Progress in 2D photonic crystal Fano resonance photonics, Progress in Quantum Electronics, (01 2014): 0. doi: 10.1016/j.pquantelec.2014.01.001
05/30/2014 27.00	Yichen Shuai, Deyin Zhao, Arvinder Singh Chadha, Jung-Hun Seo, Hongjun Yang, Shanhui Fan, Zhenqiang Ma, Weidong Zhou. Coupled double-layer Fano resonance photonic crystal filters with lattice-displacement, Applied Physics Letters, ( 2013): 0. doi: 10.1063/1.4846475
05/30/2014 26.00	Karthik Balasundaram, Parsian K. Mohseni, Yi-Chen Shuai, Deyin Zhao, Weidong Zhou, Xiuling Li. Photonic crystal membrane reflectors by magnetic field-guided metal-assisted chemical etching, Applied Physics Letters, ( 2013): 0. doi: 10.1063/1.4831657
05/30/2014 25.00	Arvinder Singh Chadha, Deyin Zhao, Santhad Chuwongin, Zhenqiang Ma, Weidong Zhou. Polarization- and angle-dependent characteristics in two dimensional photonic crystal membrane reflectors, Applied Physics Letters, ( 2013): 0. doi: 10.1063/1.4832221
05/30/2014 24.00	Yichen Shuai, Deyin Zhao, Zhaobing Tian, Jung-Hun Seo, David V. Plant, Zhenqiang Ma, Shanhui Fan, Weidong Zhou. Double-layer Fano resonance photonic crystal filters, Optics Express, (10 2013): 0. doi: 10.1364/OE.21.024582
05/30/2014 23.00	Juejun Hu, Lan Li, Hongtao Lin, Ping Zhang, Weidong Zhou, Zhenqiang Ma. Flexible integrated photonics: where materials, mechanics and optics meet [Invited], Optical Materials Express, (08 2013): 0. doi: 10.1364/OME.3.001313
05/30/2014 22.00	WeiQuan Yang, Hongjun Yang, Guoxuan Qin, Zhenqiang Ma, Jesper Berggren, Mattias Hammar, Richard Soref, Weidong Zhou. Large-area InP-based crystalline nanomembrane flexible photodetectors, Applied Physics Letters, ( 2010): 0. doi: 10.1063/1.3372635
08/12/2011 1.00	WeiQuan Yang, Rui Li, Zhenqiang Ma, Weidong Zhou. Electrical properties of stacking electrodes for flexible crystalline semiconductor photonic devices, Semiconductor Science and Technology, (09 2011): 95018. doi: 10.1088/0268-1242/26/9/095018
08/12/2011 2.00	Deyin Zhao, Hongjun Yang, Zhenqiang Ma, Weidong Zhou. Polarization independent broadband reflectors based on cross-stacked gratings, Optics Express, (04 2011): 9050. doi: 10.1364/OE.19.009050
09/03/2012 9.00	Tapas Kumar Saha, Mingyu Lu, Zhenqiang Ma, Weidong Zhou. Design of an Angle Detector for Laser Beams Based on Grating Coupling, Micromachines, (02 2012): 36. doi: 10.3390/mi3010036
09/03/2012 11.00	Hongjun Yang, Deyin Zhao, Santhad Chuwongin, Jung-Hun Seo, WeiQuan Yang, Yichen Shuai, Jesper Berggren, Mattias Hammar, Zhenqiang Ma, Weidong Zhou. Transfer-printed stacked nanomembrane lasers on silicon, Nature Photonics, (07 2012): 0. doi: 10.1038/nphoton.2012.160

- 09/03/2012 10.00 Weidong Zhou, Zhenqiang Ma, Santhad Chuwongin, Yi-Chen Shuai, Jung-Hun Seo, Deyin Zhao, Hongjun Yang, Weiquan Yang. Semiconductor nanomembranes for integrated silicon photonics and flexible Photonics, Optical and Quantum Electronics, (05 2012): 0. doi: 10.1007/s11082-012-9586-8
- 09/03/2012 8.00 Hongjun Yang, Deyin Zhao, Jung-Hun Seo, Santhad Chuwongin, Seok Kim, John A. Rogers, Zhenqiang Ma, Weidong Zhou. Broadband Membrane Reflectors on Glass, IEEE Photonics Technology Letters, (03 2012): 476. doi: 10.1109/LPT.2011.2181351
- 09/15/2013 13.00 D. Zhao, H. Yang, S. Chuwongin, J. H. Seo, Z. Ma, W. Zhou. Design of Photonic Crystal Membrane-Reflector-Based VCSELs, IEEE Photonics Journal, (12 2012): 2169. doi: 10.1109/JPHOT.2012.2227955
- 09/15/2013 14.00 Jung-Hun Seo, Jungho Park, Deyin Zhao, Hongjun Yang, Weidong Zhou, Byeong-Kwon Ju, Zhenqiang Ma. Large-Area Printed Broadband Membrane Reflectors by Laser Interference Lithography, IEEE Photonics Journal, (02 2013): 2200106. doi: 10.1109/JPHOT.2012.2236545
- 09/15/2013 15.00 Yichen Shuai, Deyin Zhao, Gautam Medhi, Robert Peale, Zhenqiang Ma, Walter Buchwald, Richard Soref, Weidong Zhou. Fano-Resonance Photonic Crystal Membrane Reflectors at Mid- and Far-Infrared, IEEE Photonics Journal, (02 2013): 4700206. doi: 10.1109/JPHOT.2013.2240446
- 09/15/2013 16.00 Weidong Zhou, Zhenqiang Ma. Breakthroughs in Photonics 2012: Breakthroughs in Nanomembranes and Nanomembrane Lasers, IEEE Photonics Journal, (04 2013): 700707. doi: 10.1109/JPHOT.2013.2250942

**TOTAL: 18**

**Number of Papers published in peer-reviewed journals:**

---

**(b) Papers published in non-peer-reviewed journals (N/A for none)**

<u>Received</u>	<u>Paper</u>
-----------------	--------------

**TOTAL:**

**Number of Papers published in non peer-reviewed journals:**

---

**(c) Presentations**

**Non Peer-Reviewed Conference Proceeding publications (other than abstracts):**

Received

Paper

- 08/12/2011 5.00 Jung-Hun Seo, Zhenqiang Ma, Jesper Berggren, Mattias Hammar, Weidong Zhou, Weiquan Yang, Hongjun Yang, Santhad Chuwongin. Frame-Assisted Membrane Transfer for Large Area Optoelectronic Devices on Flexible Substrates, IEEE Photonics Society Winter topic Meetings 2011. 10-JAN-11, . : ,
- 08/12/2011 6.00 Tapas Kumar Saha, Mingyu Lu, Huiqing Zhai, Deyin Zhao, Weidong Zhou. Design of a compact grating coupler with controllable linewidths via transverse resonance and evanescent field coupling, IEEE Photonics Society Winter Topical Meetings 2011. 11-JAN-11, . : ,
- 08/12/2011 7.00 Weiquan Yang, Hongjun Yang, Weidong Zhou, Zhenqiang Ma, Santhad Chuwongin. Flexible crystalline InP nanomembrane LED arrays, 2010 23rd Annual Meeting of the IEEE Photonics Society (Formerly LEOS Annual Meeting). 06-NOV-10, Denver, CO, USA. : ,
- 09/03/2012 12.00 Yichen Shuai, Deyin Zhao, Weiquan Yang, Weidong Zhou, Jung-Hun Seo, Zhenqiang Ma, Gautam Medhi , Robert Peale, Walter Buchwald, Richard Soref. Fano Resonance Membrane Reflectors from Mid-Infrared to Far-Infrared, IEEE Photonics Conference 2011. 25-OCT-11, . : ,

**TOTAL: 4**

**Number of Non Peer-Reviewed Conference Proceeding publications (other than abstracts):**

---

**Peer-Reviewed Conference Proceeding publications (other than abstracts):**ReceivedPaper

- 08/12/2011 3.00 Zhenqiang Ma, WeiQuan Yang, Santhad Chuwongin, Yi-Chen Shuai, Jung-Hun Seo, Deyin Zhao, Hongjun Yang, Richard Soref , Weidong Zhou. Semiconductor Nanomembranes for Integrated and Flexible Photonics, 2011 ICO International Conference on Information Photonics. 18-MAY-11, . : ,
- 08/12/2011 4.00 Zhenqiang Ma, Kan Zhang, Jung-Hun Seo, Han Zhou, Lei Sun, Hao-Chih Yuan, Guoxuan Qin, Huiqing Pang, Weidong Zhou. Fast Flexible Electronics Based on Printable Thin Mono-Crystalline Silicon, China Semiconductor Technology International Conference 2011 (CSTIC 2011). , Shanghai, China. : ,
- 09/15/2013 17.00 Deyin Zhao, Santhad Chuwongin, Hongjun Yang, Jung-Hun Seo, Jesper Berggren, Mattias Hammar, Zhenqiang Ma, Weidong Zhou. Transfer printed photonic crystal nanomembrane lasers on silicon with low optical pumping threshold, 2012 IEEE 9th International Conference on Group IV Photonics (GFP). 28-AUG-12, San Diego, CA, USA. : ,
- 09/15/2013 18.00 Deyin Zhao, Hongjun Yang, Jung-Hun Seo, Zhenqiang Ma, Weidong Zhou. Cavity design of nanomembrane MR-VCSELs on silicon, 2012 IEEE Photonics Conference (IPC). 22-SEP-12, Burlingame, CA, USA. : ,
- 09/15/2013 19.00 Santhad Chuwongin, Hongjun Yang, Jung-Hun Seo, Deyin Zhao, Yichen Shuai, WeiQuan Yang, Jesper Berggren, Mattias Hammar, Zhenqiang Ma, Weidong Zhou. Nanomembrane transfer printing for MR-VCSELs on silicon, 2012 IEEE Photonics Conference (IPC). 22-SEP-12, Burlingame, CA, USA. : ,

**TOTAL:****5****Number of Peer-Reviewed Conference Proceeding publications (other than abstracts):**

---

**(d) Manuscripts**ReceivedPaper**TOTAL:**

Number of Manuscripts:

Books	
<u>Received</u>	<u>Book</u>
TOTAL:	

<u>Received</u>	<u>Book Chapter</u>
-----------------	---------------------

TOTAL:

Patents Submitted

Patents Awarded

Awards

Graduate Students

<u>NAME</u>	<u>PERCENT SUPPORTED</u>	Discipline
Arvinder Chadha	0.23	
Yichen Shuai	0.38	
Tzu-Hsuan Chang	0.25	
Sang June Cho	0.25	
Gui Gui	0.15	
YEi Hwan Jung	0.34	
Tong Kim	0.28	
Jung-Hun Seo	0.48	
FTE Equivalent:	2.36	
Total Number:	8	

---

### Names of Post Doctorates

NAME

PERCENT SUPPORTED

**FTE Equivalent:**

**Total Number:**

---

### Names of Faculty Supported

NAME

PERCENT SUPPORTED

**FTE Equivalent:**

**Total Number:**

---

### Names of Under Graduate students supported

NAME

PERCENT SUPPORTED

**FTE Equivalent:**

**Total Number:**

### Student Metrics

This section only applies to graduating undergraduates supported by this agreement in this reporting period

The number of undergraduates funded by this agreement who graduated during this period: ..... 0.00

The number of undergraduates funded by this agreement who graduated during this period with a degree in science, mathematics, engineering, or technology fields:..... 0.00

The number of undergraduates funded by your agreement who graduated during this period and will continue to pursue a graduate or Ph.D. degree in science, mathematics, engineering, or technology fields:..... 0.00

Number of graduating undergraduates who achieved a 3.5 GPA to 4.0 (4.0 max scale):..... 0.00

Number of graduating undergraduates funded by a DoD funded Center of Excellence grant for Education, Research and Engineering:..... 0.00

The number of undergraduates funded by your agreement who graduated during this period and intend to work for the Department of Defense ..... 0.00

The number of undergraduates funded by your agreement who graduated during this period and will receive scholarships or fellowships for further studies in science, mathematics, engineering or technology fields: ..... 0.00

---

### Names of Personnel receiving masters degrees

NAME

**Total Number:**

---

### Names of personnel receiving PHDs

NAME

Yichen Shuai

Arvinder Chadha

**Total Number:**

2



---

### Names of other research staff

NAME

PERCENT SUPPORTED

**FTE Equivalent:**

**Total Number:**

---

### Sub Contractors (DD882)

1 a. University of Wisconsin - Madison

1 b. Suite 6401

21 N Park St

Madison

WI

537151218

**Sub Contractor Numbers (c):**

**Patent Clause Number (d-1):**

**Patent Date (d-2):**

**Work Description (e):**

**Sub Contract Award Date (f-1):**

**Sub Contract Est Completion Date(f-2):**

---

1 a. University of Wisconsin - Madison

1 b. Research Services and Administrative

21 N Park St.

Madison

WI

537151218

**Sub Contractor Numbers (c):**

**Patent Clause Number (d-1):**

**Patent Date (d-2):**

**Work Description (e):**

**Sub Contract Award Date (f-1):**

**Sub Contract Est Completion Date(f-2):**

---

### Inventions (DD882)

**Scientific Progress**

**Technology Transfer**

## **ARO Final Report**

**Agreement Number: W911NF0910505**

**ARO PM: Dr. Mike Gerhold**

**PI: Prof. Weidong Zhou, Univ. of Texas at Arlington**

**Sub-contract PI: Prof. Zhenqiang Ma, University of Wisconsin-Madison**

Report date: April 24, 2014

This final report consists of two reports for two periods:

**Report 1: Base Period: (For the period of Oct. 1, 2009 to Jul. 31, 2012)**

**Title: Membrane Reflector Vertical Cavity Lasers at Near- and Midwave-Infrared**

**Report 2: Add-on Period: (For the period of Aug. 1, 2012 to March 31, 2014)**

**Title: Thermally-Engineered Membrane-Reflectors for High Performance VCSELs**

### **Abstract**

We carried out both fundamental and developmental research on a novel DBR-free membrane reflector based VCSELs (MR-VCSELs), with the demonstration of 1550 nm lasing operation at room temperature. The laser consists of an InGaAsP QW based heterostructure, sandwiched in between two single-layer photonic crystal Fano resonance silicon nanomembrane reflectors. Detailed theoretical and experimental work has been carried out towards high performance single layer broadband membrane reflector demonstrations, MR-VCSEL cavity design, and optically pumped laser demonstration at room temperature. The thermally engineering membrane reflectors have also been investigated for high performance lasers.

### **Summary of Base Period (Aug. 1, 2009 to July 31, 2012):**

We have completed all the proposed research tasks as listed in the proposal, with the following major achievements: (1) Detailed investigations of single layer broadband membrane reflectors (MRs) based on Fano resonance Photonic crystal designs on silicon, with the demonstration of high performance broadband membrane reflectors (MR) at NIR and MWIR spectral bands; (2) Detailed investigations of MR-VCSEL cavity design for 1550 nm wavelength lasing; (3) InGaAsP quantum-well (QW) heterostructure design and growth, with a novel process being developed for InGaAsP QW active region nanomembrane (NM) transfer and stacking onto the bottom Si MR; (4) Successful demonstration of optically pumped 1550nm band MR-VCSELs, with the work published in Nature Photonics; and (5) Investigation and design optimization of different MR-VCSEL configurations with improved thermal performance.

### **Summary of Add-On Period (Aug. 1, 2012 to March 31, 2014):**

We have carried out all the proposed research tasks as listed in the add-on proposal. Over the last one year and seven months, we have made the following major achievements: (1) Deposition of low index thermally-conductive materials of diamond and AlN on top of Si-MR; (2) Transfer of Si-MRs on highly thermal conductive MgO substrate; (3) Demonstration of optically and electrically pumped MR-VCSELs with metal thermally-assisted structure; and (4) Incorporation of diamond layer for improved thermal conductivities for higher power handling.

**Related publications (Total 54; Journal: 21; Invited conference talks: 13; Contributed conference talks: 20)**

#### Journals

1. D. Zhao, Z. Ma and W.D. Zhou, "Field penetration and distribution in photonic crystal mirror cavities", *Opt. Express* Vol. 18, Issue 13, pp. 14152-14158, 2010.
2. Z. X. Qiang, H. Yang, S. Chuwongin, D. Zhao, Z. Ma, and W. D. Zhou, "Design of Fano broadband reflectors on SOI", *IEEE Photon. Technol. Lett.* May 23, 2010.
3. W. Yang, H. Yang, G. Qin, Z. Ma, J. Berggren, M. Hammar, R. Soref, and W. D. Zhou, "Large-area InP-based crystalline nanomembrane flexible photodetectors", *Appl. Phys. Lett.* Vol. 96, 121107 (2010).
4. W. Yang, R. Li, Z. Ma, and W. Zhou, "Electrical properties of stacked electrodes for flexible crystalline semiconductor optoelectronic devices", *Semicond. Sci. Tech.*, 26 095018 (2011).
5. D. Zhao, H. Yang, Z. Ma, and W. Zhou, "Polarization independent broadband reflectors based on cross-stacked gratings," *Opt. Express* 19, 9050-9055 (2011).
6. H. Yang, D. Zhao, J.-H. Seo, S. Chuwongin, S. Kim, J. A. Rogers, Z. Ma, and W. Zhou, "Broadband Membrane Reflectors on Glass", *IEEE Photon. Technol. Lett.* 24(6), 476-8, 2012.
7. T. Saha, M. Lu, Z. Ma, and W. Zhou, "Design of an Angle Detector for Laser Beams based on Grating Coupling", *Micromachines* (special issue on Nanophotonics), vol. 3, 36-44 (2012).
8. W. Zhou, Z. Ma, S. Chuwongin, Y.-C. Shuai, J.-H. Seo, D. Zhao, H. Yang, and W. Yang, "Semiconductor nanomembranes for integrated silicon photonics and flexible Photonics (Invited)", *Opt. Quant. Electron.*, Special Issue on Photonic Integration, DOI 10.1007/s11082-012-9586-8, 2012.
9. H. Yang, D. Zhao, S. Chuwongin, J.-H. Seo, W. Yang, Y. Shuai, J. Berggren, M. Hammar, Z. Ma and W. Zhou, "Transfer printing stacked nanomembrane lasers on silicon", *Nature Photonics* <http://www.nature.com/nphoton/journal/vaop/ncurrent/full/nphoton.2012.160.html> (one of the mostly downloaded papers; with over 60 websites reporting this work).
10. D. Zhao, H. Yang, S. Chuwongin, J.H. Seo, Z. Ma and W. Zhou, "Design of photonic crystal membrane reflector based VCSELs", *IEEE Photon. J.* vo.4(6), 2169 (2012) (DOI: 10.1109/JPHOT.2012.2227955)
11. J.-H. Seo, J. Park, D. Zhao, H. Yang, W. Zhou, B.-K. Ju, and Z. Ma, "Large-area printed broadband membrane reflectors by laser interference lithography", *IEEE Photon. J.* vol. 5(1), 2200106 (2013).
12. Y.-C. Shuai, D. Zhao, W. Yang, W. Zhou, J.-H. Seo, Z. Ma, G. Medhi, R. Peale, W. Buchwald and R. Soref, "Fano Resonance Membrane Reflectors from Mid-Infrared to Far-Infrared", *IEEE Photon. J.* 5, (1) 2200106 (2013).
13. W. D. Zhou and Z. Ma, "Breakthroughs in Photonics 2012: Breakthroughs in Nanomembranes and Nanomembrane Lasers (Invited)", *IEEE Photon. J.* vol. 5(2), 0700707 (2013).
14. Y.-C. Shuai, D. Zhao, W. Yang, W. Zhou, J.-H. Seo, Z. Ma, G. Medhi, R. Peale, W. Buchwald and R. Soref, "Fano Resonance Membrane Reflectors from Mid-Infrared to Far-Infrared", *IEEE Photon. J.* 5, (1) 2200106 (2013).
15. W. D. Zhou and Z. Ma, "Breakthroughs in Photonics 2012: Breakthroughs in Nanomembranes and Nanomembrane Lasers (Invited)", *IEEE Photon. J.* vol. 5(2), 0700707 (2013).
16. J. Hu, L. Li, H. Lin, P. Zhang, W. Zhou, and Z. Ma, "Flexible integrated photonics: where materials, mechanics and optics meet (Invited)", *Opt. Mater. Express*, vol. 3(9), 1313-1331 (2013).
17. Y. Shuai, D. Zhao, Z. Tian, J.-H. Seo, R. B. Jacobson, D. Plant, M. Lagally, S. Fan, Z. Ma, and W.D. Zhou, "Double-layer Fano resonance photonic crystal filters", *Opt. Express*, vol.21, 24582-9 (2013).

18. A. Chadha, D. Zhao, S. Chuwongin, Z. Ma, and W. Zhou, "Polarization- and angle-dependent characteristics in two dimensional photonic crystal membrane reflectors", *Appl. Phys. Lett.*, vol..103, 211107 (2013).
19. K. Balasundaram, P. K. Mohseni, Y. Shuai, D. Zhao, W. Zhou, and X. Li, "Photonic crystal membrane reflectors by magnetic field-guided metal-assisted chemical etching", *Appl. Phys. Lett.* vol..103, 214103 (2013).
20. Y. Shuai, D. Zhao, J. Seo, H. Yang, S. Fan, Z. Ma and W. Zhou, "Coupled double-layer Fano resonance photonic crystal filters with lattice-displacement", *Appl. Phys. Lett.*, vol..103, 241106 (2013).
21. W. Zhou, D. Zhao, Y. Shuai, H. Yang, S. Chuwongin, A. Chadha, J.-H. Seo, K. Wang, V. Liu, Z. Ma, and S. Fan, "Fano resonance photonic crystal nanomembrane photonics (Invited review)", *Prog. Quantum. Electron.* 38, 1-74 (2014).

#### Invited Conference talks

22. W. D. Zhou and Z. Ma, "Semiconductor nanomembranes for stacked and flexible photonics (Invited)", *Photonics West 2010, Jan. 23-28, 2010, San Francisco, CA.*
23. D. Zhao, W.D. Zhou, and Z. Ma, "Design of Dielectric Photonic Crystal Reflector Fabry-Perot Cavities", *SPIE Annual Meeting, San Diego, Aug. 2010.*
24. W. D. Zhou, Z. Ma, W. Yang, S. Chuwongin, Y. Shuai, J. Seo, D. Zhao, H. Yang, and R. Soref "Stacked crystalline semiconductor nanomembranes for 3D Si photonics (Invited)", *International Topical Meeting on Information Photonics*, May 18-20, 2011, Ottawa, Canada.
25. Z. Ma, K. Zhang, J.-H. Seo, H. Zhou, L. Sun, H.-C. Yuan, G. Qin, H. Pang and W. D. Zhou, "Fast Flexible Electronics Based on Printable Thin Mono-Crystalline Silicon (Invited)", *China Semiconductor Technology International Conference (CSTIC) 2011*, March 13-14 in Shanghai, China.
26. W. D. Zhou and Z. Ma, "Nanomembrane Heterogeneous Integration for Si Photonics and Flexible Optoelectronics (**Invited**)", 1<sup>st</sup> International Congress on Nano Science and Technology, Oct. 23-26, 2011, Dalian, China.
27. W. D. Zhou and Z. Ma, "Nanomembrane Photonics for Si Photonic Integration and Flexible Optoelectronics (**Invited**)", American Physical Society (APS) March Meeting, Feb. 27-Mar. 2, 2012, Boston, MA.
28. W. D. Zhou, Z. Ma, and H. Yang "Transfer printed photonic crystal nanomembrane lasers for integrated silicon photonics (Invited)", *Photonics West 2013, Feb. 2-7, 2013, San Francisco, CA.*
29. W. D. Zhou, Z. Ma, and H. Yang "Transfer Printed Semiconductor Nanomembrane Photonics (Invited)", 2013 TMS Annual Meeting & Exhibition, Mar. 3-7, 2013, San Antonio, TX.
30. Z. Ma and W.D. Zhou, "Transferrable semiconductor nanomembranes and their versatile applications (Invited)", SPIE Micro- and Nanotechnology Sensors, Systems, and Applications Conference 2013, April 29 - May 3, 2013, Baltimore, MD.
31. W. D. Zhou, and Z. Ma, "Transfer printed photonic crystal nanomembrane lasers on silicon (Invited)", Integrated Photonics Research, Silicon and Nano Photonics (IPR) conference, July 14-19, 2013, Rio Mar Beach Resort, Rio Grande, Puerto Rico.
32. W. D. Zhou, and Z. Ma, "Transfer printed nanomembranes for silicon photonics, flexible electronics and optoelectronics (Invited)", *SPIE Micro+Nano Materials, Devices and Applications Conference*, Dec. 8-11 2013, RMIT University, Melbourne, Australia.
33. W. D. Zhou, and Z. Ma, "Fano resonance membrane reflector surface emitters and filters on silicon (Invited)", *Photonics West 2014, Feb. 1-6, 2014, San Francisco, CA.*
34. W.D. Zhou and Z. Ma, "Nanomembrane integrated silicon photonics and flexible optoelectronics (Invited)", *Integrated Photonics in OSA FiO/LS annual meeting 2014*, Oct. 19-23, 2014, Tucson , AZ.

#### Contributed Conference Talks

35. W. Yang, H. Yang, S. Chuwongin, J.-H. Seo, Z. Ma, J. Berggren, M. Hammar, and W. D. Zhou, "Frame-Assisted Membrane Transfer for Large Area Optoelectronic Devices on Flexible Substrates", *IEEE Winter 2011 Topicals on Photonic Materials and Integration Architecture*, Jan. 10-12, 2011, Keystone, CO.
36. T. Saha, M. Lu, H. Zhai, D. Zhao, W. D. Zhou and Z. Ma, "Design of a compact grating coupler with controllable linewidths via transverse resonance and evanescent field coupling", *IEEE Winter 2011 Topicals on Photonic Materials and Integration Architecture*, Jan. 10-12, 2011, Keystone, CO.

37. S. Chuwongin, W. Yang, H. Yang, W.D. Zhou, and Z. Ma, "Flexible Crystalline InP Nanomembrane LED Arrays", *IEEE Photonics Society Annual Meeting, Denver, Nov. 8-11, 2010*.
38. Y.-C. Shuai, D. Zhao, W. Yang, W. Zhou, J.-H. Seo, Z. Ma, G. Medhi, R. Peale, W. Buchwald and R. Soref, "Fano Resonance Membrane Reflectors from Mid-Infrared to Far-Infrared", *IEEE Photonics Meeting 2011*, Arlington, VA, Oct. 9-13, 2011.
39. J.-H. Seo, J. Park, D. Zhao, H. Yang, W.D. Zhou, B.-K. Ju, and Z. Ma, "Print transferrable large-area broadband membrane reflectors by laser interference lithography", *Nanotech Conference & Expo, 2012*, June 18-21, 2012 - Santa Clara, CA.
40. D. Zhao, S. Chuwongin, H. Yang, J.-H. Seo, J. Berggren, M. Hammar, Z. Ma and W. Zhou, "Transfer printing photonic crystal nanomembrane lasers on silicon with low optical pumping threshold (POSTDEADLINE paper)", *9<sup>th</sup> International Conference on Group IV Photonics*, Aug. 29-31, 2012, San Diego, CA.
41. D. Zhao, H. Yang, J.-H. Seo, Z. Ma, and W.D. Zhou, "Cavity Design of Nanomembrane MR-VCSELs on silicon", *IEEE Photonics Conference (IPC2012)*, Sept. 23-27, San Francisco, CA.
42. S. Chuwongin, H. Yang, J.-H. Seo, D. Zhao, W. Yang, J. Berggren, M. Hammar, Z. Ma, and W.D. Zhou, "Nanomembrane Transfer Printing for MR-VCSELs on silicon", *IEEE Photonics Conference (IPC2012)*, Sept. 23-27, San Francisco, CA.
43. Y. Shuai, D. Zhao, Z. Tian, J.-H. Seo, R. B. Jacobson, D. Plant, M. Lagally, S. Fan, Z. Ma, and W.D. Zhou, "Stacked Fano Resonance Photonic Crystal Nanomembrane High-Q Filters", *IEEE Photonics Conference (IPC2012)*, Sept. 23-27, San Francisco, CA.
44. M. Rakhmanov, T. D. Miler, A. Gribovskiy, S. Chuwongin, D. Zhao, and W.D. Zhou, "Sub-wavelength Diffraction Losses in a Silicon Nano-Patterned Membrane Reflector", *IEEE Photonics Conference (IPC2012)*, Sept. 23-27, San Francisco, CA.
45. A. Gribovskiy, T. D. Miller, and M. Rakhmanov, S. Chuwongin, D. Zhao, and W. Zhou, "Wide-Angle Polarization-Dependent Diffraction in a Silicon Nano-Patterned Membrane Reflector", *Texas section American Physical Society Fall 2012 Meeting*, Lubbock, TX, Oct. 25-27, 2012.
46. J.-H. Seo, H. Zhou, D. M. Paskiewicz, M. G. Lagally, W. Zhou, Z. Ma, "15-GHz Flexible Microwave Thin-Film Transistors on Plastic (Tu2C1)", *IEEE MTT International Microwave Symposium (IMS)*, June 2-7, 2013, Seattle, WA, USA.
47. W. Fan, D. Zhao, S. Chuwongin, J.-H. Seo, H. Yang, J. Berggren, M. Hammar, Z. Ma, and W. Zhou, "Electrically-pumped membrane-reflector surface-emitters on silicon", *IEEE Summer Topicals Meeting on Micro- and Nano-cavity Integrated Photonics*, July 8-10, 2013, Hilton Waikoloa Village, Waikoloa Hawaii, USA.
48. Y. Shuai, D. Zhao, J.-H. Seo, H. Yang, S. Fan, Z. Ma and W. Zhou, "Transfer Printed Nanomembrane High-Q Filters Based on Displaced Double-Layer Fano Resonance Photonic Crystal Slabs", *IEEE Photonics Conference 2013*, Sept. 8-12, 2013, Hyatt Regency Bellevue, Bellevue, Washington, USA.
49. W. Fan, D. Zhao, S. Chuwongin, J.-H. Seo, H. Yang, J. Berggren, M. Hammar, Z. Ma, and W. Zhou, "Fabrication of Electrically-pumped Resonance-cavity Membrane-reflector Surface-emitters on Silicon", *IEEE Photonics Conference 2013*, Sept. 8-12, 2013, Hyatt Regency Bellevue, Bellevue, Washington, USA.
50. A. Chadha, D. Zhao, and W. Zhou, "An all dielectric broadband high transmission efficiency circular polarizer", *Photonics West 2014*, Feb. 1-6, 2014, San Francisco, CA.
51. A. Chadha, Y. Shuai, and W. Zhou, "High Performance Second-Order Surface-Normal Vertical to In-plane Optical Coupler", *Photonics West 2014*, Feb. 1-6, 2014, San Francisco, CA.
52. Y. Shuai, K. Balasundaram, P. K. Mohseni, , D. Zhao, H. Yang, X. Li, and W. Zhou, "High performance photonic crystal membrane reflectors by magnetically guided metal-assisted chemical etching", *Photonics West 2014*, Feb. 1-6, 2014, San Francisco, CA.
53. D. Zhao, A. Chadha, S.-C. Liu, H. Yang, Z. Ma, and W. Zhou, "High performance surface-normal photonic crystal membrane reflectors for in-lane light coupling", *IEEE Photonics Conference 2014*, Oct. 12-16, 2014, Hyatt Regency La Jolla, San Diego, CA (submitted).
54. D. Zhao, S.-C. Liu, J. H. Seo, Y. Liu, Z. Ma, and W. Zhou, "Thermally engineered photonic crystal membrane reflectors based on transferred nanomembranes", *IEEE Photonics Conference 2014*, Oct. 12-16, 2014, Hyatt Regency La Jolla, San Diego, CA (submitted).

## Detailed Report for Base Period (Aug. 1, 2009 to July 31, 2012)

### (1) Completed design of high performance top and bottom membrane-reflectors (MR) for laser cavity resonance around 1550 nm.

Shown in Fig. 1(a) is a three-dimensional (3D) schematic view of a complete MR-VCSEL structure, with the cross-sectional 2D view shown in Fig. 1(b). For practical laser cavity design, two types of MR reflectors will be used. The bottom mirror will be processed directly on an SOI wafer without using any transfer process. The bottom single layer patterned Si NM MR reflector is sandwiched in between two low-index oxide buffer layers (denoted as “oxide-Si-oxide”, or OSO configuration, based on the reflector vertical confinement). The top reflector will be first processed on SOI, and then transferred onto the top of an InP QW active region, with air and oxide as its two buffer layers above and below the patterned SiNM reflector (denoted as “air-Si-oxide”, or ASO configuration). Detailed work has been carried out to understand the impacts of the buffer layer index and the layer thicknesses. Shown in Fig. 1(c) and (d) are the simulated spectra results for both top and bottom MR reflectors considering the presence of buffer layers in the active laser cavity.

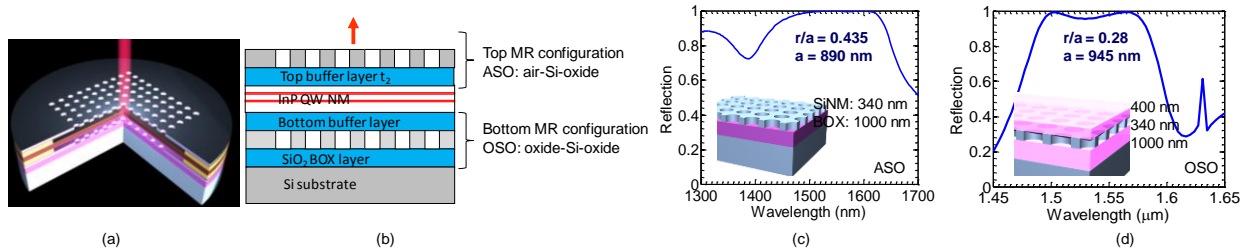


**Fig. 1** Design of membrane reflectors (MR) for MR-VCSEL cavity at 1550 nm: (a, b) Schematics of MR-VCSEL, with ASO top reflector and OSO bottom reflector designs; (c, d) Simulated reflection spectra for top ASO and bottom OSO MR reflectors, with optimized buffer layer configurations. Note:  $r$ ,  $a$  are air hole radius and lattice constant, respectively. The SiNM and oxide layer thicknesses are also shown.

### (2) Demonstration of high performance broadband membrane reflectors (MR) at NIR and FIR spectral bands.

Membrane reflector (MR) design was done based on finite difference time-domain (FDTD) simulation and rigorous coupled-wave analysis (RCWA) techniques. A sketch of Si MR on glass is shown in Fig. 2(a). Shown in Fig. 2(b-d) are the simulated reflector performances for designs at three different wavelength bands. All designs are based on suspended (in air) Si MR configurations. Broadband reflection with 100% peak reflection is possible for all designed wavelength bands, with the optimal selection of lattice parameters and Si thicknesses.

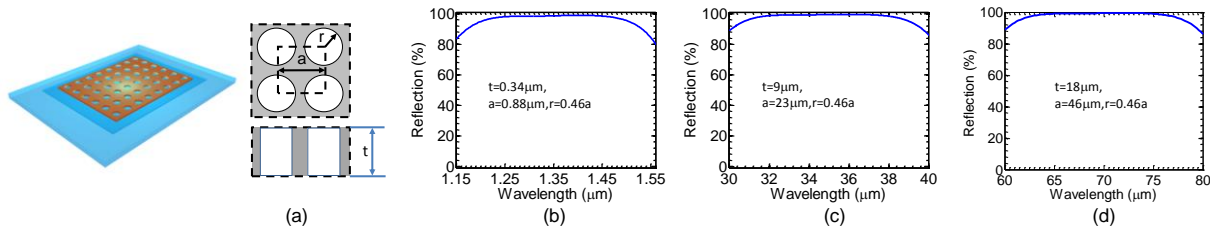


**Fig. 2** (a) 3D sketch of a Si membrane reflector with a patterned 2D air hole square lattice photonic crystal structure on glass substrate; (b-d) Simulated reflector performances for designs at three different wavelength bands. Key design parameters shown are Si thickness ( $t$ ), lattice constant ( $a$ ), and air hole radius ( $r$ ).

Large-area Si MRs were fabricated based on photolithography and deep reactive-ion etching (DRIE) process on SOI substrates. The patterned Si membrane structures were later released by selective buffered HF (BHF) etching of buried oxide (BOX) layer underneath, and transferred onto foreign substrates, based on wet transfer technique. Shown in Fig.

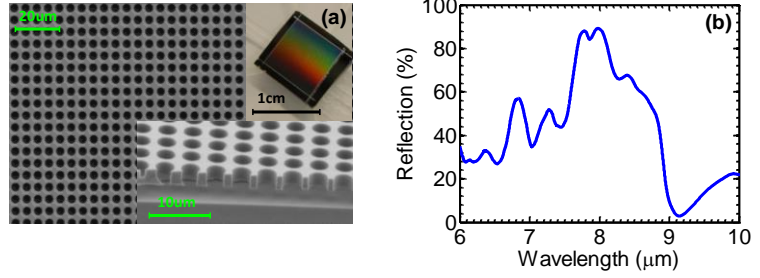


**Fig. 3** (a) A scanning-electron micrograph (SEM) of the MR top view, along with insets showing a SEM cross-sectional view and a micrograph of the complete MR structure; (b) Measured reflection spectrum for a mid-IR MR reflector with reflection band centered at 8 μm.

3 is the device structure and measured reflection spectra for a MR structure with design center-wavelength of 8 μm. Both top and cross-sectional scanning electron micrograph (SEM) images are shown in Fig. 3(a), along with a 1 x 1 cm<sup>2</sup> MR reflector micrograph shown in the inset. Shown in Fig. 3(b) is a reflection spectrum measured at 23.6° off-surface-normal using a 15x, 0.4NA reflecting lens associated with a micro-Fourier Transform Infrared (FTIR) spectrometer. Notice that the peak reflection band at ~ 8 μm overlaps the strong absorption band associated with the buried oxide layer of the SOI used for the reflector, therefore the peak reflection of the MR at this wavelength band will be limited by the oxide absorption. Improved reflection would thus be possible by removing the buried oxide underneath the Si MR.

### (3) MR transfer process development and optimization.

In the current integration scheme of MR-VCSEL, we first transfer the top MR on glass substrate, as shown in Fig. 4(a). The top MR on glass substrate will be then stacked on top of the InGaAsP QW layer to form the complete MR-VCSEL cavity. It was a challenging issue to have a high quality large area NM transfer with excellent reflection performance and high manufacturing yield. We have been working with our subcontractors on this issue. It seems processes have been improved and optimized, with much better yield in high quality top MR transfer process. Additionally, based on over temperature investigations, we have also started working on top MR designs with center wavelength shifted from 1550nm to 1500nm, for lower temperature operation. Shown in Fig. 4 (b) are the latest experimental results of the measured and simulated reflection spectra before transfer (on SOI Si substrate). SEM images of fabricated top MR on SOI are also shown in Fig. 4 (c,d). As seen from these results, the peak reflection values of these fabricated MR samples are relatively low (~90% reflection), which might due to the fabrication errors related to the E-beam patterning and RIE processes. We are working on these issues by scanning the parameters and calibrating Si dry etching (RIE) recipe.

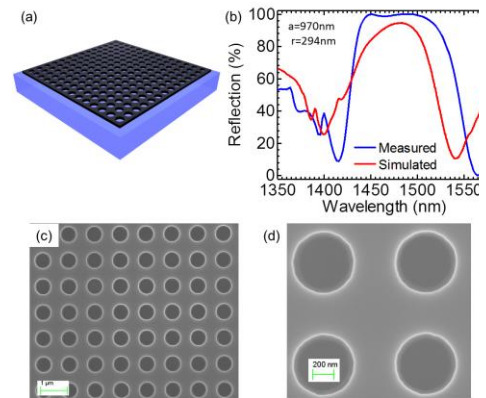


**Fig. 4** (a) A schematic of the top MR on glass; (b) Measured and simulated top MR reflection results; and (c,d) SEM images of fabricated top MR via E-beam lithography.

### (4) Experimental demonstration of high performance



### MR reflectors on Si and transferred to glass/PET substrates.

For MR on SOI (Fig. 5(a)), we have demonstrated 99% reflection over a 50 nm bandwidth around 1550 nm, with theoretical bandwidth over 100 nm expected for both polarizations. SiNM transfer process is being developed to ensure high-quality transfer and to ensure high performance reflectors based on transferred SiNM on PET substrates. Shown in Fig. 5(b) is a patterned SiNM MR reflector transferred to a glass substrate. The measured reflection spectra before and after transfer are shown in Fig. 5(c). Notice that little degradations were observed, with un-optimized transfer process. Both MR on SOI and MR transferred to glass will be used as the bottom and top reflectors, respectively, in the final MR-VCSEL cavity. More experimental work is being carried out on optimizing the oxide buffer layer deposition and high quality MR reflector transfer.

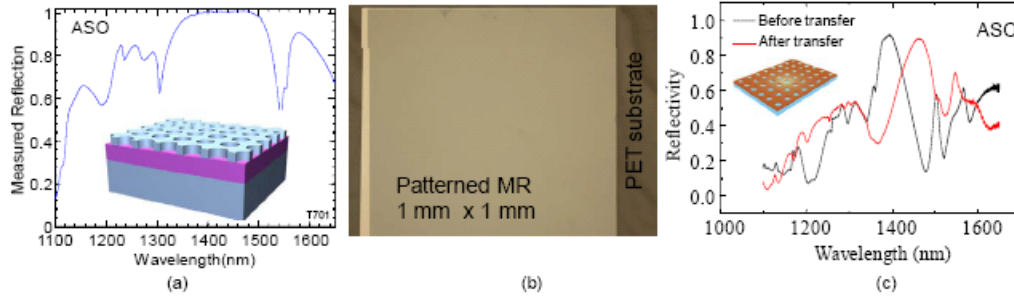


**Fig. 5** Experimental results of membrane reflectors: (a) Measured reflection spectrum for a bottom reflector on SOI before top oxide buffer layer deposition (ASO configuration); (b) A top-view image and (c) measured reflection spectra for the top reflector before and after SiNM transferred onto PET substrate. Notice the peak reflection only reduced slightly after transfer. The sample used here has a narrow reflection band and the spectral bandwidth is optimized at 1550 nm.

### (5) MR-VCSEL cavity design.

As shown in Fig. 6(b), low index buffer layers will be inserted in between the high-index SiNM bottom MR, the high-index InGaAsP QW NM active region, and the high-index SiNM top MR. Detailed simulations have been carried out to optimize the cavity design for (a) desired cavity spectral resonance alignment with active region light emission spectral location; and (b) desired cavity spatial overlap between the active region QW location and the anti-node location of the MR-VCSEL cavity resonance standing wave. MR-VCSEL cavity configuration is near the final optimal design. Such a design is shown in Fig. 6, for the complete cavity resonance simulations, with different buffer layer thickness  $t_2$  shown in Fig. 6(b).

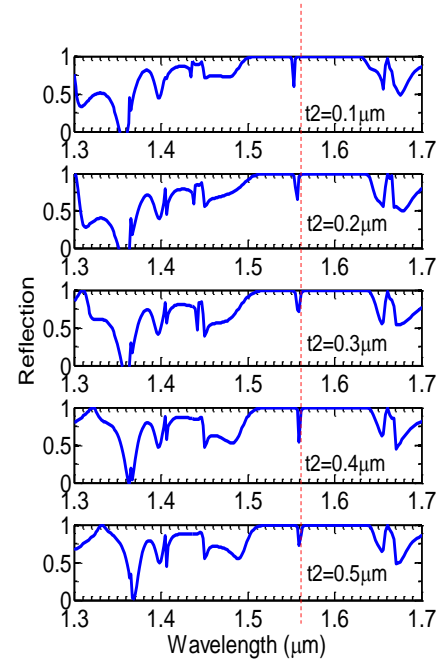


**Fig. 6** Cavity design optimizations: the impact of the low-index buffer layer thickness, for layer  $t_2$  shown in Fig. 2(b).

### (6) InP-based QW heterostructure design, growth, and



**NM transfer/stacking process development.** Two types of QW heterostructures have been designed, with total cavity thickness of one  $\lambda$  (wavelength). The PL peak locations are around 1547 nm. An InGaAs etch stop/sacrificial layer was used for the release of top InP QW active region. It was found that the PL quantum efficiency improves after release of InP substrate, mostly due to better thermal performance. In addition, based on the metal frame-assisted membrane transfer (FAMT) process, large area InP NMs have been successfully released and transferred, for the stacking of optical and/or electrical-pumped MR-VCSEL process. Shown in Fig. 7(a) and (b) are the schematic and a micro-image of the InP QW NM transferred onto a bottom MR on SOI substrate, respectively. As shown in Fig. 7(c), improved PL emission efficiency was also observed for QW active region stacked on top of bottom MR reflectors, due to the photo-recycling effect. Further spectral and spatial alignments between the InP QW active layer and bottom MR reflector are being carried out for the desired cavity resonance matching.

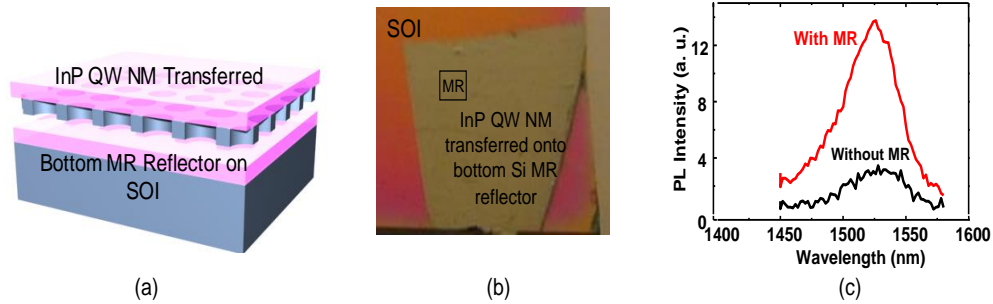


**Fig. 7** Experimental results of InGaAsP QW active region transfer and stacking on top of a bottom MR reflector: (a) Schematic of InP QW NM transferred on top of the bottom MR reflector on SOI; (b) A micrograph of a piece of InP QW NM transferred on top of the bottom Si MR reflector; and (c) Measured photoluminescence (PL) results for the InGaAsP QW heterostructure transferred onto SOI substrate with patterned MR reflectors.

## (7) MR-VCSEL Cavity Design

Once two good mirrors with high reflectivity are obtained, a multi-layer SiMR/QW/SiMR MR-SEL cavity can be built up based on semiconductor nanomembrane (NM) printing transfer process. Here, we need to decide the cavity resonant mode by selecting a suitable cavity length, i.e., the thickness of the buffer layers between SiMR and QW before we fabricate the real device. Then, we also need to investigate and understand the properties of this cavity mode, such as quality factor ( $Q$ ), field distribution, and confinement factor. Good cavity mode with high  $Q$  and high confinement factor is pursued to reduce the gain threshold for lasing. Fig. 8(a) shows the schematic of one MR-VCSEL example for low temperature design. The inset displays the square lattice air hole PC structure with  $a=860\text{nm}$ . The air hole has Larger air hole radius is used in both top and bottom MR,  $r_t=0.46a$ ,  $r_b=0.45a$ , and  $n_f=1.2$ . Buffer layer thickness  $t_2$  and  $t_4$  can be tuned to adjust the cavity mode location. To make the field distribution more symmetric inside cavity, another  $\text{SiO}_2$  layer with  $t_6=400\text{nm}$  is used. In simulation, a periodical boundary condition is used, i.e., the lateral dimension is infinite. Fig. 8(b) demonstrates the reflections of top and bottom MR, where the high reflection ( $>98\%$ ) covers the wavelength range from 1420 to 1530nm.

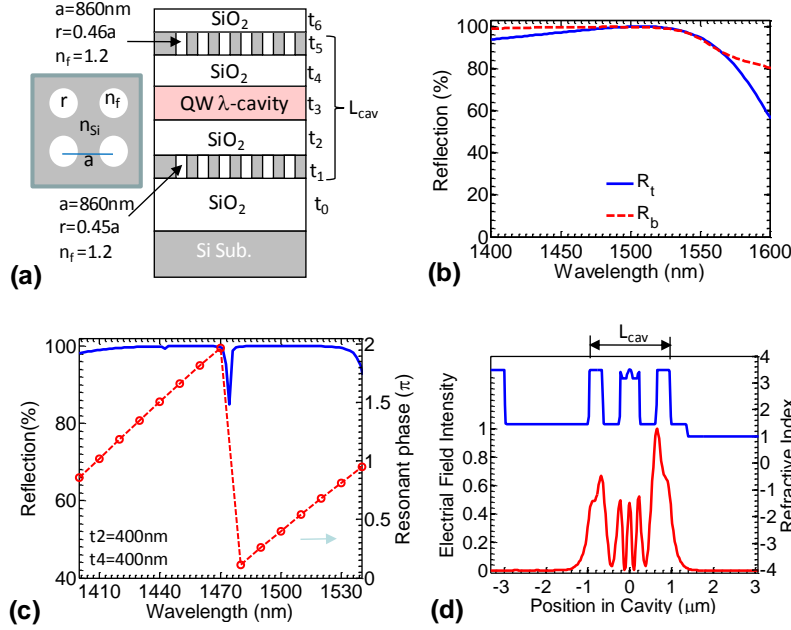


**Fig. 8** Characteristics of designed MR-VCSEL cavity. a, MR-VCSEL cavity structure configuration. b, Reflections of top and bottom MR. c, Calculated cavity resonance mode based on cavity reflection and phase resonant condition. d, Field distribution of cavity mode.

We use two ways to decide the cavity mode. The first one is to calculate the reflection of the whole cavity structure. From the dips located into the high reflection band range, we can easily find the cavity mode according to its resonant transmission property. The reflection of MR-VCSEL with  $t_2=t_4=400\text{nm}$  is plotted in Fig. 8(c) with the blue line, which is calculated using rigorous coupled-wave analysis (RCWA) method. We can find the dip is located at  $1478\text{nm}$ . To confirm this cavity mode, a method based on phase resonant condition (total phase change of one round-trip in cavity is equal to integer times of  $2\pi$ ) is used to decide cavity mode. The phase calculation details can be found in our earlier publication (*Opt. Express* 18, 14152 (2010)). After got the reflection phase change ( $\phi$ ) of the top and bottom MR, the resonant cavity mode can easily decide without  $t_2$  and  $t_4$  parameter scan. The phase of mode in cavity is shown in Fig. 8(c) with red dash dotted line, which is limited in the range of  $[0, 2\pi]$ . One can find the mode located at  $1478\text{nm}$  has a  $m \cdot 2\pi$  phase change.

Next, we investigate the properties of quality factor and field distribution of this cavity mode. By employing FDTD (MIT Meep program), a short temporal gaussian pulse is used to excite the cavity modes and the quality factor of the cavity mode  $1478\text{nm}$  is calculated to be 4300 according to  $Q=\text{Re}(\omega)/-2\text{Im}(\omega)$ . Then a longer temporal gaussian pulse is used to excite only this cavity mode and the stable field is recorded after the source is turned off for a long time. The E-field of the standing wave distribution is demonstrated in Fig. 8(d) with red line, where the cavity index profile is also plotted with blue line. One can see one of E-field peak is located at QW well region and we calculated the confinement factor is about  $\Gamma=5.6\%$  according to  $\int_{QW} E^2 dv / \int_{cav} E^2 dv$ .

It is worthy to note is that the field intensity inside top and bottom MR is relatively larger. This is because of reflection mechanism of guided resonant effect, i.e., guided mode excitation in Si membrane. Although the field intensity inside SiMR is large, it does not give rise to much cavity loss and absorption loss.

In practice, top and bottom MR always have different PC lattice,  $a_t \neq a_b$ , and the cavity has finite size. In this case, instead of simple periodical boundary condition, perfect matched layer (PML) boundary condition is used in FDTD simulations. Here we studied two cavity configurations with a square size  $\sim 22 \times 22 \mu\text{m}^2$ , 1)  $a_t=860\text{nm}$ ,  $r_t=0.46a_t$ ,  $a_b=880\text{nm}$ ,  $r_b=0.45a_b$ ,  $t_2=380\text{nm}$ ,  $t_4=420\text{nm}$ ; 2)  $a_t=980\text{nm}$ ,  $r_t=0.28a_t$ ,  $a_b=880\text{nm}$ ,  $r_b=0.45a_b$ ,  $t_2=370\text{nm}$ ,  $t_4=470\text{nm}$ , in which the cavity modes are designed for low and room temperature, respectively. The reflection of the cavity is obtained by calculating the reflected flux outside the cavity and the resonant mode is found through the Fourier transfer of  $E(t)$  of one monitor inside the cavity. The reflection and resonant spectra are plotted together with blue solid and red dashed lines, as shown in Fig. 9. One can find the cavity modes match well between the dip in reflection spectrum and the peak in resonant spectrum. In addition, the estimated Qs of these two cavity modes are  $\sim 1100$ . The linewidths of dip and peak in these two spectra are not narrow because of the relatively short time steps in FDTD simulation. (The simulation time and structure size are limited by the memory and CPU number). So far, once the buffer layer thickness is chose, all the key parameters of cavity structure will be fixed.

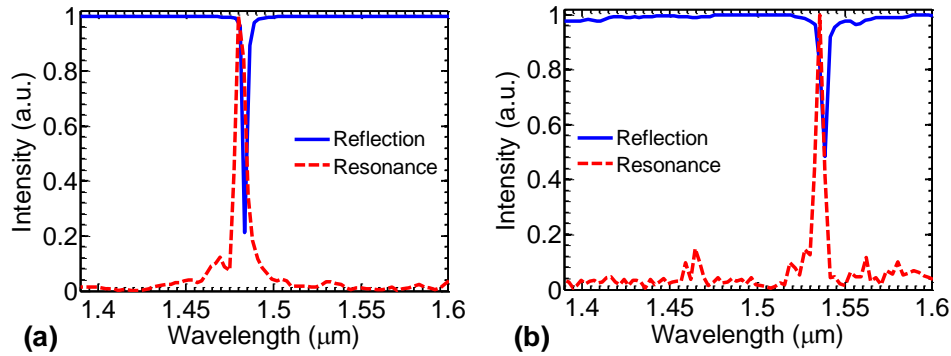


**Fig. 9** Cavity mode of MR-VCSEL cavity with finite size. Reflections (blue lines) and resonant (red dash lines) spectra of MR-VCSEL: (a) for Low T at  $\lambda=1478\text{nm}$  and (b) for Room T at  $\lambda=1540\text{nm}$ .

#### **(8) Demonstration of optically pumped MR-VCSELs, with the work being published in Nature Photonics.**

One of the major milestones for this project is the successful demonstration of optically pumped MR-VCSELs working under low and room temperature operation conditions. The work was published in Nature Photonics, which received worldwide attention--over 60 websites reported our work. Comprehensive characterizations have been carefully performed on these devices to further investigate and analyze MR-VCSEL performance.

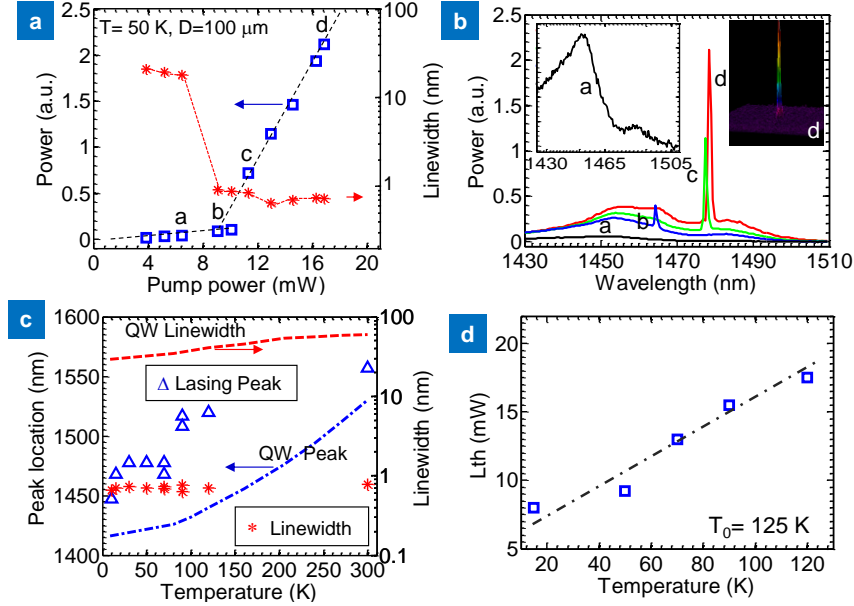


**Fig. 10** Low temperature MR-VCSEL performances with LT Design MRs. a, Laser output power at the lasing wavelength and lasing linewidth versus the input pump power. The sample was cooled at  $T = 50$  K and pumped with a chopped continuous wave (CW) green laser. The actual absorbed power is difficult to estimate. The lateral lasing cavity diameter is  $D = 100$   $\mu\text{m}$  (inset), with total vertical cavity thickness of 2373 nm. b, Measured spectral output of the MR-VCSEL at three pump power levels, below threshold (a), at threshold (b) and above thresholds (c, d). The spontaneous emission below threshold (at pump power point a) is shown in the inset. Also shown in the inset is the far field (FF) image above threshold (point d). c, Measured lasing spectral peak locations and linewidths at different temperatures. Also shown are the measured QW PL peak locations and linewidths at different temperatures. d, Measured lasing threshold power for different temperatures. A characteristic temperature  $T_0$  is extracted to be 125 K.

The L-L plot (light output for different pump powers) and the corresponding spectral linewidths are shown in Fig. 10(a), for a LT design MR-VCSEL device with active area  $D$  of 100  $\mu\text{m}$  at ambient temperature  $T$  of 50 K. The threshold pump power is  $\sim 8$  mW, or  $0.32$  KW/cm<sup>2</sup>. Notice the actual absorbed power should be much less, though it is difficult to estimate here. The measured spectral linewidths change from 30 nm below threshold to 0.6 - 0.8 nm above threshold. Measured spectral outputs are shown in Fig. 10(b), for pump powers below, at, and above thresholds (points (a, b, c, d) at L-L curve). For better visibility, the spectrum below threshold is amplified and shown in the inset of Fig. 10(b). The lasing spectral linewidth is  $\sim 8$  Å. Also shown in Fig. 10(b) is a measured far-field image for the MR-VCSEL biased above threshold (point (d) at L-L curve). Very collimated single mode output is evident at this bias level, for this MR-VCSEL with relatively large lateral active dimension ( $D = 100$   $\mu\text{m}$ ). The relative peak location shift from bias (b) to (c, d) is mostly related to mode hopping and temperature rise inside the active region at higher pump power levels. This is also evident in Fig. 10(c), where the lasing peak locations concentrate at about 1478 nm and 1520 nm for operation temperatures below and above 80K, respectively.

The lasing spectral linewidth remains relatively constant at 0.6 - 0.8 nm. MR-VCSEL device was characterized at different temperatures up to 120 K, mostly limited by the MR reflector bandwidth. While the QW emission peak has a red-shift at a rate of 0.43 nm/K with rising temperature, the MR reflector has a blue-shift at a rate of 0.067 nm/K. For this set of low

temperature MR-VCSEL samples, the measured temperature dependent lasing threshold is shown in Fig. 10(d), where the extracted characteristic temperature is 125 K. Another set of MR-VCSEL was also demonstrated for quasi-c.w. mode lasing at room temperature, with both the top and the bottom MRs centered at 1550 nm band (RT design). The optical characteristic results are shown in Fig. 11(a). The pump threshold is 18 mW, very similar to the low temperature threshold at 120 K (Fig. 10(d)). The lasing spectral linewidth is  $\sim 0.9$  nm. Currently this MR-VCSEL thermal performance is limited by the use of the low index  $\text{SiO}_2$  layer, which has poor thermal conductivity. By replacing this oxide layer with other low index materials having higher thermal conductivity, such as  $\text{Al}_2\text{O}_3$ , AlN, or diamond films, we expect much better thermal performance and much higher lasing efficiency.

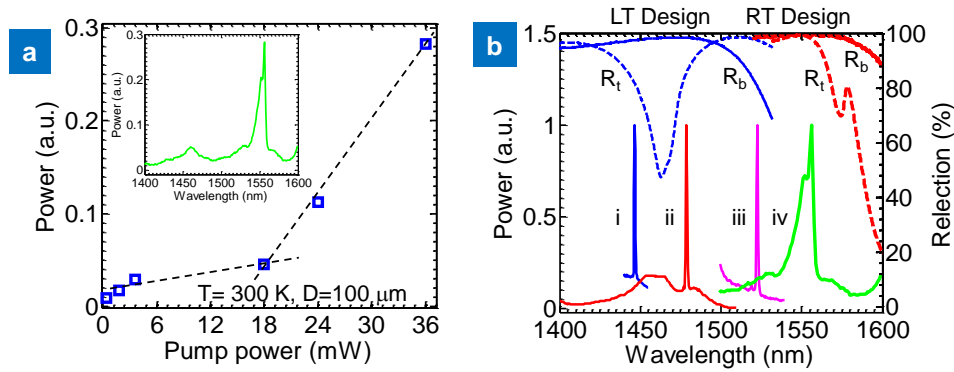


**Fig. 11** RT Design MR-VCSELs and multi-spectral lasing. a, Laser L-L curve at room temperature for RT Design MR-VCSEL device. b, Measured MR-VCSEL spectral outputs at different temperatures for both LT and RT Designs: (i)  $T = 10$  K; (ii)  $T = 50$  K; (iii)  $T = 120$  K; and (iv)  $T = 300$  K. Portions of measured top ( $R_t$ ) and bottom ( $R_b$ ) reflection spectra are also shown for both LT and RT design.

Multi-wavelength MR-VCSEL arrays can be realized in these planar ultra-compact MR-VCSEL structures, by varying the photonic crystal lattice parameters of both top and bottom MRs. Here we demonstrate different lasing wavelengths based on MRs with LT design and RT design. Measured spectral outputs are shown in Fig. 11(b). For LT design cavity, lasing wavelengths of 1448 nm (at 10 K), 1478 nm (at 50 K), and 1520 nm (at 120 K) were obtained at different temperatures. For RT design cavity, lasing wavelength of 1557 nm was obtained. These lasing wavelengths match well with the cavity resonances based on different designs.

#### (9) MR-VCSEL cavity thermal performance investigation and choice of buffer layer materials.

Since the buffer layer used in our MR-VCSEL structure is either  $\text{SiO}_2$  or air, both of them have relatively poor thermal conductivities. To further improve lasing cavity thermal performance, we have designed/simulated heat sink for the thermal effect control in MR-VCSEL structure. Shown in Fig. 12(a) illustrates that a 60nm thick heat sink layer is embedded between InGaAsP QW active layer and bottom buffer  $\text{SiO}_2$  layer. In order to maintain the same cavity optical property, the effective optical length of the combination of heat sink layer and 250nm bottom buffer  $\text{SiO}_2$  layer was designed as same as pure  $\text{SiO}_2$  buffer layer of 380nm thick. The simulated thermal distribution plots are shown in Fig. 12 (b). Significant improved thermal dissipation capabilities were evident for the cases with thin layers of 60nm  $\text{Al}_2\text{O}_3$  or diamond materials.

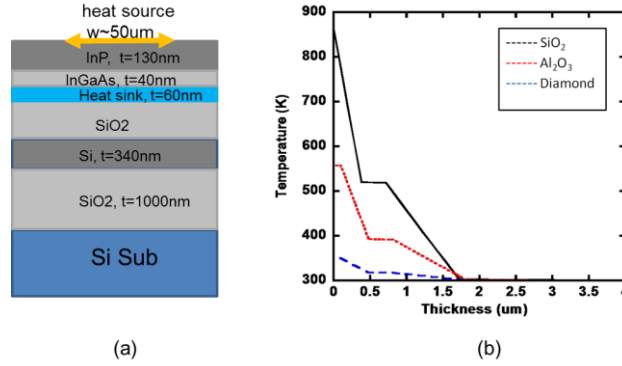


**Fig. 12** Thermal effect control (a) Cross-section schematics of complete MR-VCSEL with 60nm heat sink layer between InGaAs QW and SiO<sub>2</sub>; and (b) Simulated thermal distribution (temperature) over thickness.

After investigation of various buffer materials with high thermal conductivities, including diamond, AlN and Al<sub>2</sub>O<sub>3</sub> shown in Table 1, we prepared bottom MR samples coated with diamond. The diamond materials were provided by sp3<sup>TM</sup> Diamond Technologies Inc. As shown in Fig. 13(a), 280 nm thick diamond was coated on top of MR. The SEM image showed polycrystal type of diamond with a rough surface. A poor reflection was measured on this sample as shown in Fig. 13(b) along with calculated Fast Fourier Transform (FFT) results.

**Table. 1** Thermal performance of different materials.

Materials	Refractive Index	Thermal Conductivity (W·m <sup>-1</sup> ·K <sup>-1</sup> )	Thermal Expansion Coefficient (10 <sup>-6</sup> /°C)
Si	3.48	130	2.62
Ge	4.275	58	5.70
SiO <sub>2</sub> /Glass	1.48	1.1	15.70
Quartz	1.46	12	7.64
SiN	1.98	30	3.3
GaAs	3.374	56	5.0
GaN	2.3	130	5.60
InP	3.172	68	4.60
InGaAs	3.44	5	5.66
Diamond	2.384	(900-2320)	1.26
PET(plastic)	1.45	0.23	39
Al <sub>2</sub> O <sub>3</sub>	1.746	26	8.1
AlN	2.15	285	
Air	1	0.045	1750

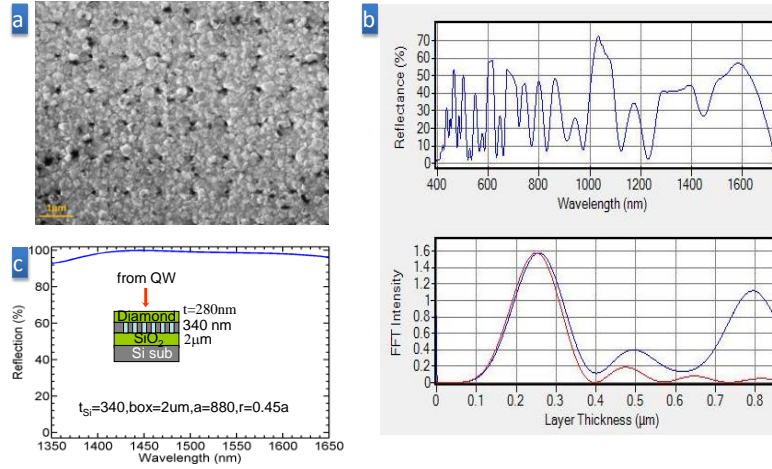
Fig. 14 shows one type of designs with no low index buffer layer between QW and bottom MR. Since silicon itself has a pretty high thermal conductivity of 130 W·m<sup>-1</sup>·K<sup>-1</sup>, the bottom Si NM MR can serve as a heat distribution material. One potential cavity design is illustrated in Fig. 14(a), with all related design parameters listed. The cavity properties were then carefully simulated based on this configuration. The top MR keeps the same design as before, while the bottom MR is different because QW on bottom MR is a high index medium, i.e., the incident medium has a huge difference, changing from SiO<sub>2</sub> to QW. So we tuned the design parameters to get a matched bottom MR. The reflection spectra of top and bottom MR are shown in Fig. 14(b). Their high reflection (>96%) range covers from around 1480 nm to 1590 nm, which is sufficient for cavity lasing at room temperature. A much enhanced cavity factor of ~8000 is



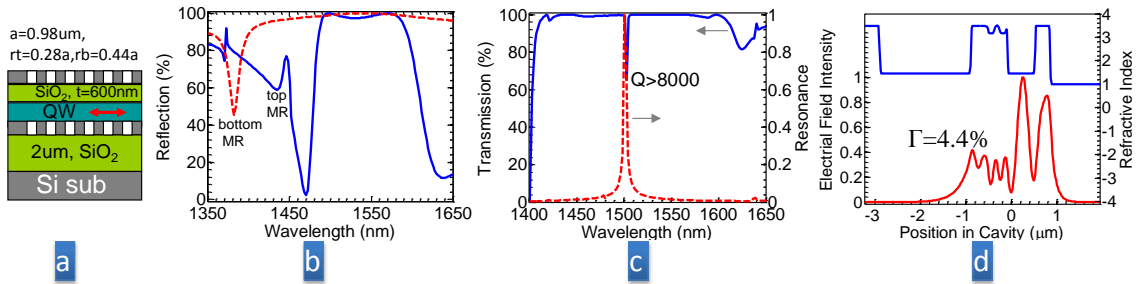
obtained for such cavity, compared with  $\sim 4000$  in case of the presence of  $\text{SiO}_2$  buffer layer, as shown in Fig. 14(c). On the other hand, the confinement factor (4.4% in

Fig. 14(d)) is a little bit reduced due to its asymmetry of such cavity compared with the symmetric structure with buffer layers (with confinement factor of 5.6%). We will continue the design optimizations to improve the cavity confinement factor and other performances.

More investigation is being carried out to further improve the overall thermal property, and especially for the MR-VCSEL operated under electrical injection.



**Fig. 13** Diamond coating and performance (a) An SEM image of 280nm thick diamond coated on MR; (b) Measured reflection and FFT intensity of diamond/MR; and (c) Simulated reflection spectrum of diamond/MR.



**Fig. 14** MR-VCSEL design without bottom buffer layer for improved thermal performance. (a) Schematic of cross-section view of MR-VCSEL structure; (b) Calculated reflection spectra of bottom/top MRs; (c) Calculated cavity resonance mode and transmission result, with a cavity factor of  $\sim 8,000$ ; and (d) Electrical field distribution in the cavity, with a 4.4% confinement factor obtained.

## Detailed Report for Add-on Period: (For the period of Aug. 1, 2012 to March 31, 2014)

### (1) Deposition of low index thermally-conductive materials of Diamond and AlN on top of Si-MR;

To investigate oxide-free Si-MRs by replacing top low index SiO<sub>2</sub> layer with other low index highly thermal conductive materials, such as AlN, ZnO, MgO, etc. Firstly, from simulation, we investigate the impact on the Si-MRs reflection since these materials have higher refractive index than SiO<sub>2</sub>, and found a good MR designs for using diamond ( $n \sim 2.38$ ) or AlN ( $n \sim 2.3$ ) as top buffer layer. Fig. 1 (a) shows the structure sketch of Si-MR with Diamond or AlN, where the thicknesses of the diamond or AlN buffer, Si, SOI box are  $\sim 240$  nm,  $340$  nm,  $2\ \mu\text{m}$ , respectively. The reflection of the Si-MR (PC lattice constant  $a=880$  nm and the air hole radius  $r=0.45a$ ) is shown in the Fig. 1(b). One can see a broad high reflection band covering from  $1430 - 1560$  nm with reflection greater than 98%. Note that, in this design, the light source is incident from QW region since it will be the real case in fabrication.

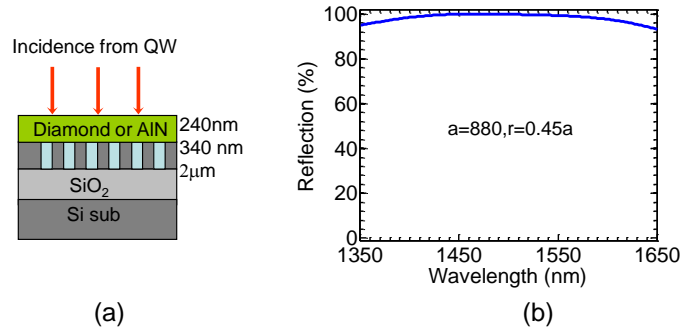


**Fig. 1** (a) Sketch of Si-MR with  $\sim 240\text{nm}$  diamond or AlN as good thermal buffer layer; (b) The reflection of Si-MR with the PC lattice constant  $a=880$  nm and air hole radius  $r=0.45a$ . Here also considering the air hole partial filling of diamond or AlN, an effective index of  $n_f=1.2$  was used in simulation.

According to the above design, we fabricated bottom Si-MR on  $340$  nm SOI wafer. Then a thin layer of diamond is coated on these bottom MR samples. The diamond materials were provided by sp3<sup>TM</sup> Diamond Technologies Inc. Shown in Fig. 2 (a) is the SEM of  $280$  nm thick diamond coated on top of MR. The SEM image showed poly-crystal type of diamond with a very rough surface. Fig. 2(b) shows a poor measured reflection after the diamond coating (dashed red line). And the rough surface is bad for further process such as QW disk transferring on it.

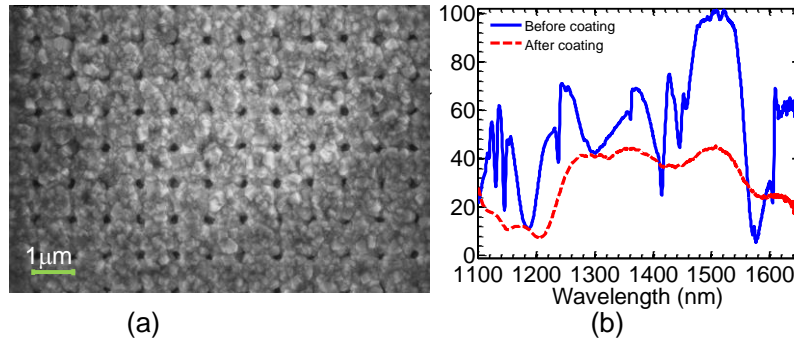


**Fig. 2** Si-MR with diamond coating and performance (a) An SEM image of  $280\text{nm}$  thick diamond coated on MR; (b) Measured reflections of before (blue solid line) and after diamond coating (dashed red line).



To improve the reflection and surface performances of such thermal MRs, we prepared another Si-MR ( $a=880\text{nm}$ ,  $r=0.45a$ ) with  $300\text{nm}$  AlN coating (AlN growth in Prof. Jiang's Lab of Texas Tech University). Fig. 3 (a) and (b) show the SEM of the Si\_MR before and after AlN coating, respectively. Comparing with diamond coating, one can see AlN coating gives much flatten MR surface. The measured reflections of Si-MR with before (blue solid line) and after (dashed red line) AlN coating are shown in Fig. 3(c). We can see the reflection after AlN coating doesn't degrade, while the reflection spectral change arises from the high index AlN coating. Fig. 3(d) shows the comparison between the measured (blue solid line) and simulated (dashed red line) reflections of this Si-MR with AlN buffer layer. They matched well, which indicates AlN will be a good candidate used for a thermal buffer layer in MR-VCSEL cavities.

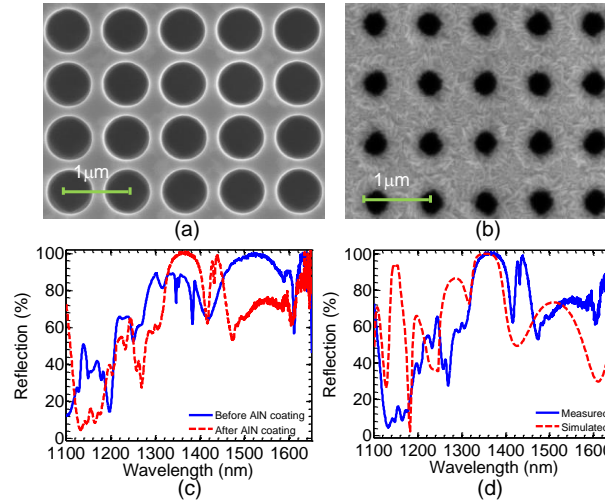


**Fig. 3** Si-MR SEMs (a) without and (b) with  $300\text{nm}$  AlN coating; (c) Measured reflections of before (blue solid line) and after diamond coating (dashed red line); (d) Measured (blue solid line) and simulated (dashed red line) reflections of Si-MR with AlN coating.

After fabrication and optical performance investigation, we further check the thermal properties of this Si-MR from thermal simulation and testing. First, we use Ansys software to simulate the temperature rising in a half MR-VCSEL cavity, as shown in Fig. 4(a). The heat generates from the InGaAsP QW region and the heat sink ( $T=300\text{K}$ ) is set at the bottom Si-MR. Fig. 4(b) shows the temperature rises for using  $\text{SiO}_2$ , AlN and diamond as buffer layer, respectively. Since the diamond has the best thermal conductivity ( $1000\sim 2000 \text{ W}\cdot\text{m}^{-1}\cdot\text{K}^{-1}$ ), the corresponding maximum  $T$  at QW center is the lowest.

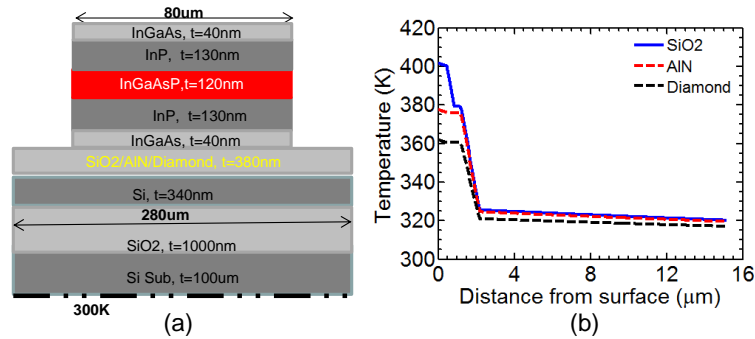


**Fig. 4** (a) Structure sketch of half MR-VCSEL, where the shown thickness and width of each layer are used in Ansys simulation; (b) The temperature rising along vertical center line of cavity for using  $\text{SiO}_2$  (blue solid line), AlN (dashed red line) and diamond buffer layer (dashed black line), respectively.

Secondly, we also test the thermal conductivity of different thin film and bulk materials by using  $3\omega$  technique. Fig. 5 (a) shows the testing setup including 1) a look-amplifier which can produce  $1\omega$  AC electrical signal and detect the  $3\omega$  AC signal generated from the thermal metal pads due to the thermal

resistance change with temperature; 2) Whetstones bridge consisting of three fixed and one adjustable resistances; 3) samples deposited with metal line (length=3.5mm and width=25 $\mu$ m) on its surface, as shown in Fig. 5(b). The metal line can work as a resistance heater and resistance thermometer simultaneously. After getting 1 $\omega$  and 3 $\omega$  electrical signal ( $v_\omega$ ,  $v_{3\omega}$ ) at different frequency signal, for example shown in Fig. 5(c) of bulk Si, we can calculate the thermal conductivity of the bulk Si. Our measured thermal conductivity value is around 145 W $\cdot$ m $^{-1}$ ·K $^{-1}$ , which is very close to reference. For thin film samples, we need to compare it with a reference sample that is the same bulk material as substrate. In Table 1, we summary our measured samples including bulk material, such as Si, glass, AlN, and MgO; thin film, such as SiO $_2$  on Si, Si $_3$ N $_4$  on Si, and AlN on SOI. All the measured values matched the references.

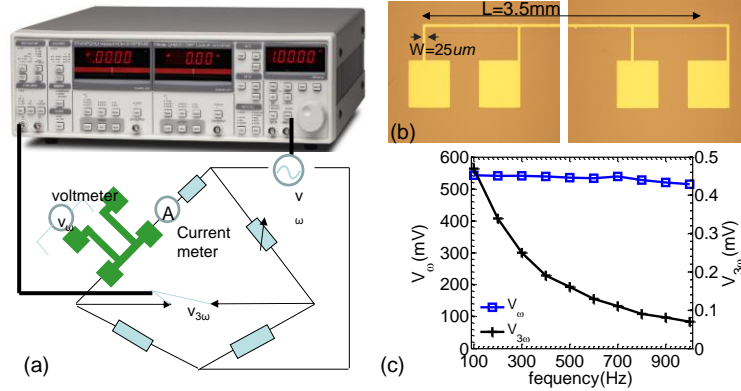


**Fig. 5** (a) Three omega ( $3\omega$ ) thermal conductivity testing setup; (b) Image of metal line deposited on the surface of the sample; (c) Measured  $\omega$  and  $3\omega$  electrical signal ( $v_\omega$ ,  $v_{3\omega}$ ) of bulk Si sample as function of frequency  $\omega$ .

**Table 1** Measured thermal conductivity of different materials.

		Substrate Thickness (mm)	Thermal Conductivity (W/m-K)	Reference (W/m-K)
Bulk Substrate	Si	0.6	145.573	139
	Glass	1.0	0.961	0.9-1.1
	AlN	0.8	276.435	285
	MgO	0.6	44.765	30-60
Thin film	SiO $_2$ on Si	400	1.488	1.5
	Si $_3$ N $_4$ on Si	400	2,464	2-3
	AlN on SOI	340	17.88	10-20

In addition, we indirectly investigate the thermal performance the SiO $_2$ , AlN and diamond substrates. We transfer some QW disks with p- and n- metal ring together on these three different substrates, then test the PL peak shift with different current injection. As shown in Fig. 6 (a) and (b) are PL spectra of the InGaAsP QW on diamond and AlN substrate, respectively. The PL peak location clearly shifts to longer wavelength as increasing the current, which are plotted together as a function of current in Fig. 6(c). Comparing the reference of QW on SOI with 370nm SiO $_2$  in between, the PL peak location shift of QW on AlN substrate is the lowest one due the better heat

spread, while that of QW on diamond is close to the reference. The reason comes from the rough surface of diamond, as see the SEM of diamond (upper) and AlN (lower) substrate in Fig. 6 (d). The rough surface makes a bad contact to QW, i.e. bad heat spread.

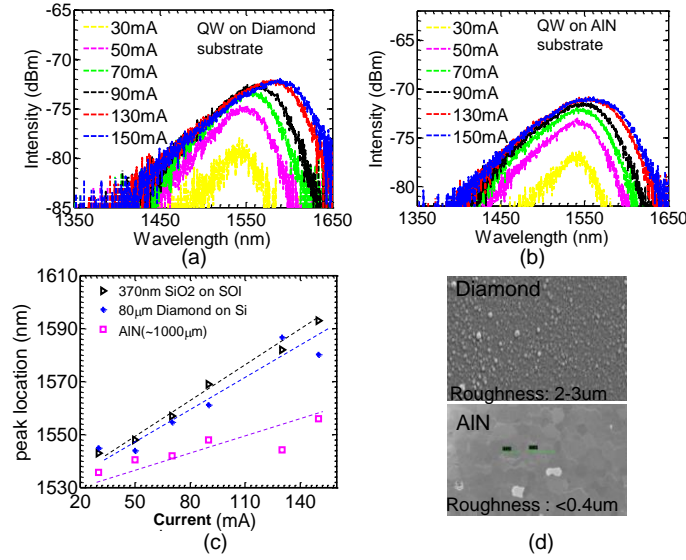


**Fig. 6** PL spectra of InGaAsP QW at different current (a) QW on diamond substrate; (b) QW on AlN substrate; (c) PL peak location vs current; (d) SEM of diamond (upper) and AlN (lower) substrates.

## (2) Transfer of Si-MRs on highly thermal conductive MgO substrate.

Except for replacing the SiO<sub>2</sub> buffer layer by AlN or diamond to improve the thermal issue in the MR-CVSEL cavity, we also replace the SOI substrate as higher thermal conductive materials, such as MgO ( $\sim 35 \text{ W} \cdot \text{m}^{-1} \cdot \text{K}^{-1}$ ) or Al<sub>2</sub>O<sub>3</sub> ( $\sim 26 \text{ W} \cdot \text{m}^{-1} \cdot \text{K}^{-1}$ ), which have relatively higher refractive index  $n \sim 1.74$  (comparing to SiO<sub>2</sub> index of 1.5). We have designed two kinds of thermal Si-MRs sitting on Al<sub>2</sub>O<sub>3</sub> substrate using Al<sub>2</sub>O<sub>3</sub> as buffer layer, shown in Fig. 7(a), and AlN as buffer layer, shown in Fig. 7(b). Both of them have a broad high reflection ( $R > 97\%$ ) bandwidth greater than 150nm with the center wavelength around 1600nm.

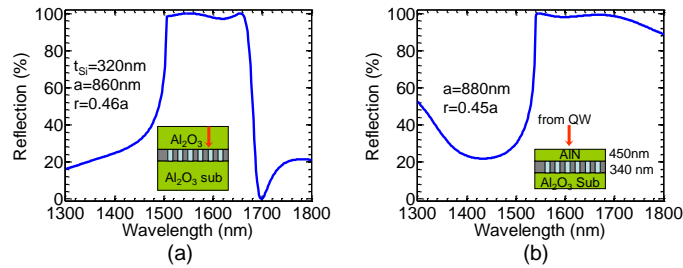


**Fig. 7** Simulated reflection spectra of Si-MRs (a) sitting on Al<sub>2</sub>O<sub>3</sub> substrate with Al<sub>2</sub>O<sub>3</sub> as buffer, and (b) sitting on Al<sub>2</sub>O<sub>3</sub> substrate with AlN as buffer. The structure parameters used in simulation are shown in the above figures. Considering the air hole partial filling of Al<sub>2</sub>O<sub>3</sub> and AlN, an effective index of  $n_f = 1.2$  is used.

To transfer Si-MR on MgO, we fabricated a Si-MR on 340 nm SOI wafer first with PC parameters  $a = 890 \text{ nm}$ , and  $r = 0.44a$ . Fig. 8(a) shows the SEM of the Si-MR before transfer. The reflection is measured and shown (blue solid line) in Fig. 8(c) with the simulated (dashed red line) together. They match well. Then we transfer this Si-MR on MgO substrate. Shown in Fig. 8(b) is the micrograph image of the transferred whole Si-MR piece sitting on MgO substrate. The

measured and simulated reflection spectra are shown in Fig. 8(d), which demonstrates both the Si-MR optical performance and fabrication quality are good.

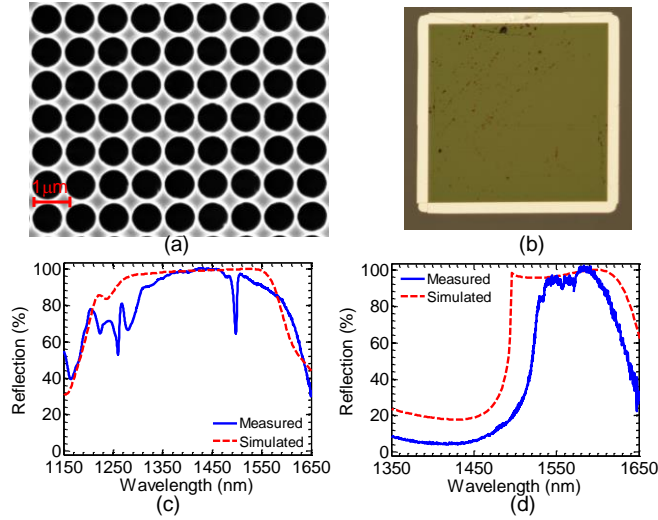


**Fig. 8** (a) SEM of Si-MR with  $a=890\text{nm}$  and  $r=0.44a$  before transfer; (b) Micrograph image of transferred Si-MR on MgO substrate; The measured (blue solid line) and the simulated (dashed red line) reflection spectra of Si-MR before (c) and after transfer (d).

### (3) Demonstration of optically and electrically pumped MR-VCSELs with metal thermally-assisted structure.

Along with separate investigation the thermal performance of Si-MR, we also have investigated the thermal performance of MR-VCSELs with whole cavity and half cavity (without top MR) by using metal-assisted method. Fig. 9 (a) shows the 3D sketch of an optically pumped half cavity with metal coating outside the QW mesas. So the heat from QW can laterally spread through the metal. The micrograph images of the real devices with and without metal coating are shown in Fig. 9(b) and (c), respectively. And the measured PL spectra under different pumping levels are illustrated in Fig. 9(d) and (e). The PL peak values are collected and plot as function of pumping power in Fig. 9(f). One can see as pumping power increase from 1mW to 10mW, the PL peak shift of the device with metal coating is about 4nm, while without metal assistance, the PL peak shifts about 8nm. Therefore, the metal coating indeed improves the heat spread although its effect is not good as the expected. The reason comes from the larger dimension size in lateral direction, which be confirmed from the sequent thermal simulation in Fig. 10.

Fig. 10 (a) shows the simulated structure where QW with diameter of  $80\mu\text{m}$  is sitting on  $\text{SiO}_2$  substrate and the gold coating outside the QW edge. The temperature field distributions are shown in Fig. 10(b) for the structures with (lower) and without (upper) gold coating. As shown in Fig. 10(c) and (d) are the temperature rises along the horizontal top surface and the vertical center in the cavity. To show clearly the T rise near the QW surface region, the marked zone in Fig. 10(d) is amplified in Fig. 10(d). From the simulation, we can find the T doesn't reduce too much at the present of metal coating due to the longer heat path in the horizontal direction then the vertical direction. The simulation results agree well with the measured results in Fig. 9.

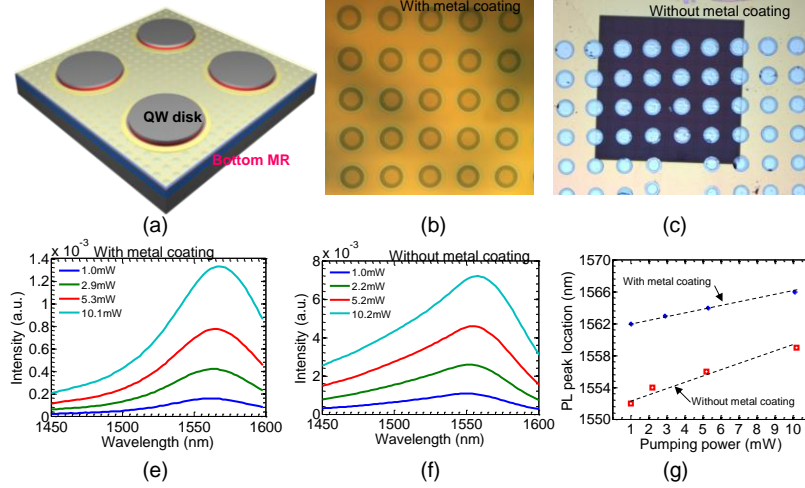


**Fig. 9** (a) 3D sketch of half MR-VCSEL with metal coating outside QW; (b) and (c) micrograph images of real devices with and without metal coating; (d) and (e) the PL spectra of the two devices in (b) and (c) at different optical pumping power; (f) The PL peak location vs pumping power for devices with (red square dot line) and without (blue star dot line) metal coating.

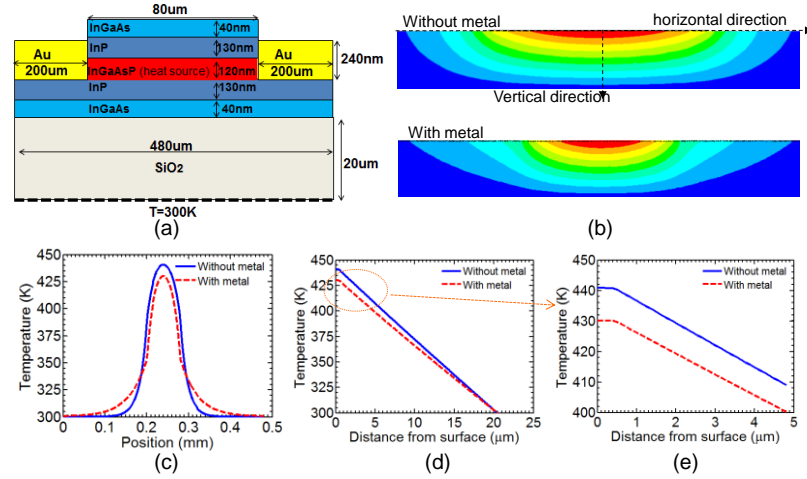


**Fig. 10** (a) Structure sketch of half MR-VCSEL with surround metal coating, where the shown thickness and width of each layer are used in Ansys simulation; (b) The temperature distributions of the half cavity without (upper) and with (lower) metal coating; The temperature rises: (c) along the vertical center line of cavity, (d) along the horizontal top surface line; (e) The zoom-in region marked in (d). The blue solid line and red dashed line represent the without and with metal cases respectively.

From the results shown in Fig. 9 and 10, one can see the metal connecting QWs and the heat sink can indeed reduce the heat effect, which is further confirmed by our electrically pumped devices with metal interconnect among QWs. Shown in Fig. 11(a) and (b) are SEMs of two real EP devices with and without metal interconnect. The tested EL spectra of the QW mesa with 50μm diameter are displayed in Fig. 11(c) and (d), respectively. The electroluminescence (EL) peak values as a function of inject current are plotted in Fig. 11(e) to clearly show the EL shift. From the slopes one can see, with metal interconnect, the EL shift of the QW is much slower than that of without interconnect due to the faster heater spread.



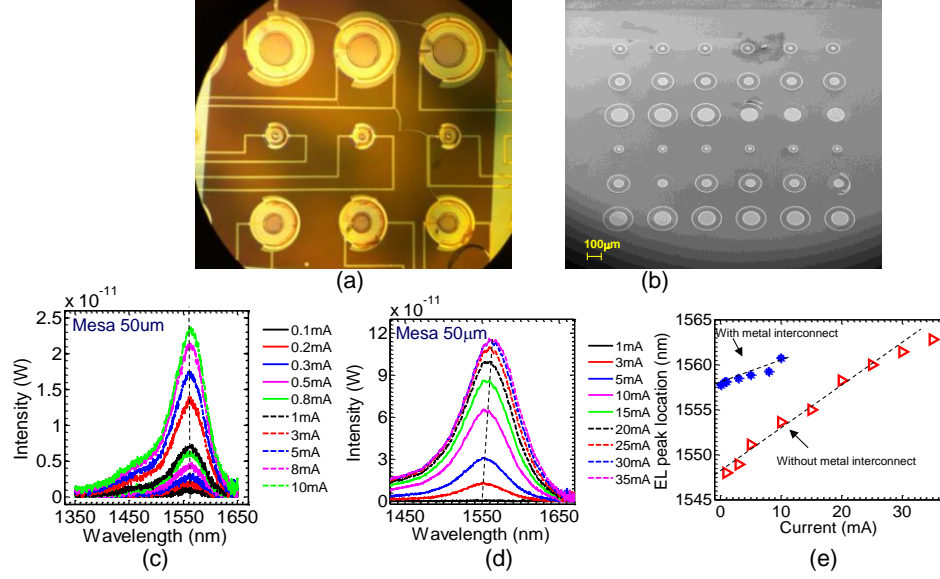


**Fig. 11** Micrograph images of real devices (a) with and (c) without metal interconnect; (c) and (d) the PL spectra of the two devices in (b) and (c) at different current injection; (f) The PL peak values vs current for the devices with (blue star dot line) and without (red triangle dot line) metal interconnect.

We also fabricated a whole electrical pumped MR-VCSEL device and investigated its performances. Shown in Fig. 12 (a) is the schematic of a complete EP Si-based MR-VCSEL cavity with intra-cavity ring contact and interconnect. The fabrication was carried out as follows. Top p- and bottom n-ring contacts were first formed on the double step mesas of p-i-n QW structure. Plasma-enhanced chemical vapor deposition (PECVD) of  $\text{SiO}_2$  and reactive ion etching (RIE) process were performed to electrically isolate the contacts from each other. InGaAsP QW heterostructure was then released and transferred onto the bottom Si-MR, subsequently, interconnect metal and contact pads were formed on bottom Si-MR and SOI substrate, in order to further fix the mesas, and also facilitate wire-bonding and mounting on chip-on-carriers. Fig. 12 (b) shows the half-cavity device on bottom Si-MR. The Si-MR/QW/Si-MR cavity was finally built by another PDMS transfer of a top Si-MR onto the top of the transferred InGaAsP QW disks. A completed electrical-pumped MR-VCSEL is shown in Fig. 12 (c).

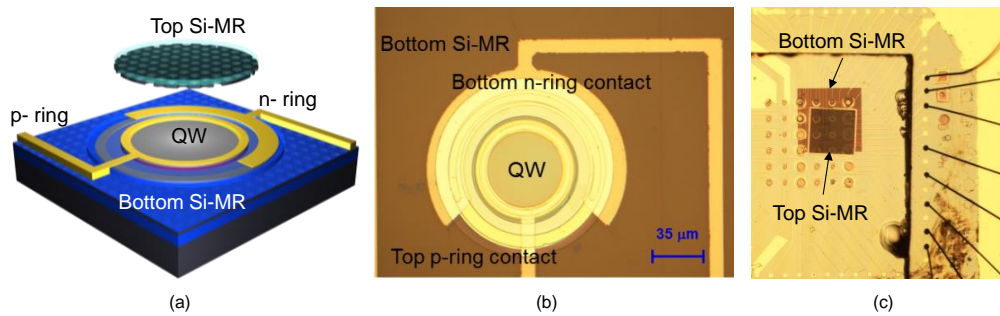


**Fig. 12** (a) Schematic of a complete electrically-pumped silicon-based membrane-reflector VCSEL (MR-VCSEL) cavity with intra-cavity ring-contacts formed on the p-i-n InGaAsP QW disk, which is sandwiched in between two single layer Si Fano resonance photonic crystal membrane reflectors (Si-MRs), stacked on a Si substrate; (b) A micrograph image of a fabricated electrical-pumped device before top Si-MR placement; and (c) A microscope image of the complete device arrays, with wire-bonding made to devices under test on chip-on-carrier.

Fig. 13 (a, b) show SEM images of the bottom-MR before and after PECVD deposition of 360 nm  $\text{SiO}_2$  on top of patterned Si-MR layer, respectively. As shown in Fig. 13 (c), the measured reflection

spectrum covers a broad high reflection band, which matches well with the designed one. For top Si-MR, we first release the fabricated pattern from the box layer and then transfer it onto a transparent glass substrate. To form the full cavity, we transfer the glass substrate holding the Si-MR onto the top of transferred QW disks.

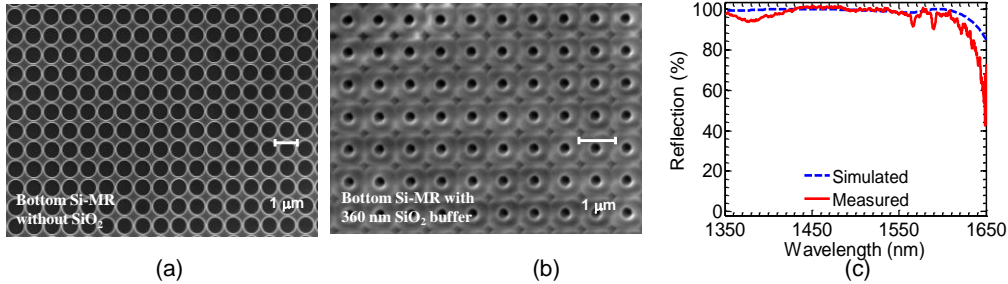


**Fig. 13** Bottom Si-MR on SOI: (a, b) SEM images of the fabricated single layer bottom Si-MR before and after PECVD deposition of 360 nm SiO<sub>2</sub> on top of patterned Si-MR layer; and (c) Measured and simulated reflection spectra for the bottom Si-MR with 360 nm SiO<sub>2</sub> deposited on top.

The room-temperature EL spectral characteristics of this device had been studied. As shown in Fig. 14 (a) is the measured light-current-voltage (L-I-V) curves, where saturation is observed at higher bias currents. Fig. 14 (b) shows the measured EL spectra for the device before (half cavity) and after (full cavity) top Si-MR placement under bias current of 1 mA. We see much reduced spectral linewidth and much increased peak intensity under the same bias current level, due to resonant cavity effects. Besides narrower spectral linewidth and enhancement of the spontaneous emission, the device takes advantages of the microcavity effects to superior directionality of emission. As shown in Fig. 14 (c) is the measured angle-dependent EL spectra, only a single emission peak at normal direction is significant, additional mode was observed at longer wavelengths with increased detect angle. Work is on-going towards the demonstrations of electrically-pumped MR-VCSELs.

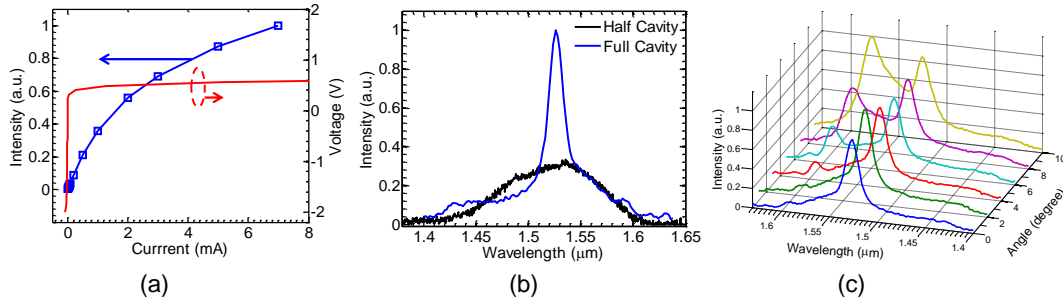


**Fig. 14** Room temperature electrically-pumped MR-VCSEL performance: (a) Measured light-current-voltage (L-I-V) curves; (b) Measured electroluminescence (EL) spectra for the device under bias of 1 mA before (half cavity) and after (full cavity) top Si-MR placement; (b) Measured EL spectra of the device in dependence on the angle under bias current of 1 mA.

#### (4) Incorporation of diamond layer for improved thermal conductivities for higher power handling.

For further using diamond to improve the thermal issue considering its best heat spread capability, we propose some new MR design incorporation of diamond for high power laser application. Shown in Fig. 15(a) is the sketch of QW on a thermal material substrate and Fig. 15(b) shows the temperature rise along the vertical center line for different substrates. One can see the diamond is best one to be used as a heat sink or a heater spreader. So, using a thick (~500μm) diamond layer as a top and bottom heat spreader, we proposed a high power VCSEL laser cavity structure with Si-MR as top and bottom mirrors, as shown in Fig. 15(c). This design

is suitable for optically pumped vertical-external-cavity surface-emitting-laser with even high power output.

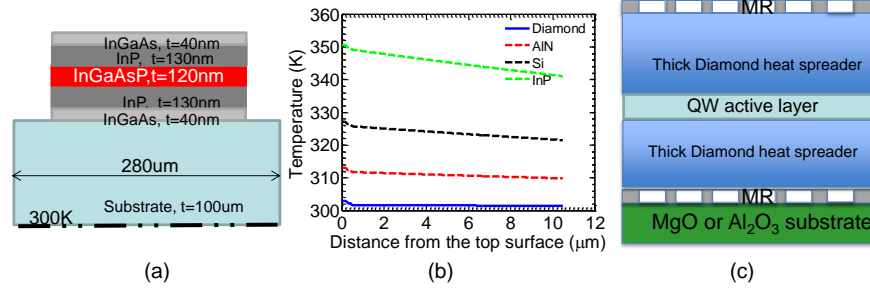


**Fig. 15** (a) Structure sketch of QW on thermal materials substrate, where the shown thickness and width of each layer are used in Ansys simulation; (b) The temperature rises along the vertical center line; (c) The sketch of vertical-external-cavity surface-emitting-laser cavity consisting of two Si-MRs, diamond heat spreader, and QW.

To demonstrate the thermal Si MR idea proposed in Fig. 15(c), we first designed the Si-MR on diamond with incident light from diamond substrate. Using membrane transfer technique, we transferred Si membrane from SOI to the diamond substrate. Fig. 16(a) and (b) show the SEM of

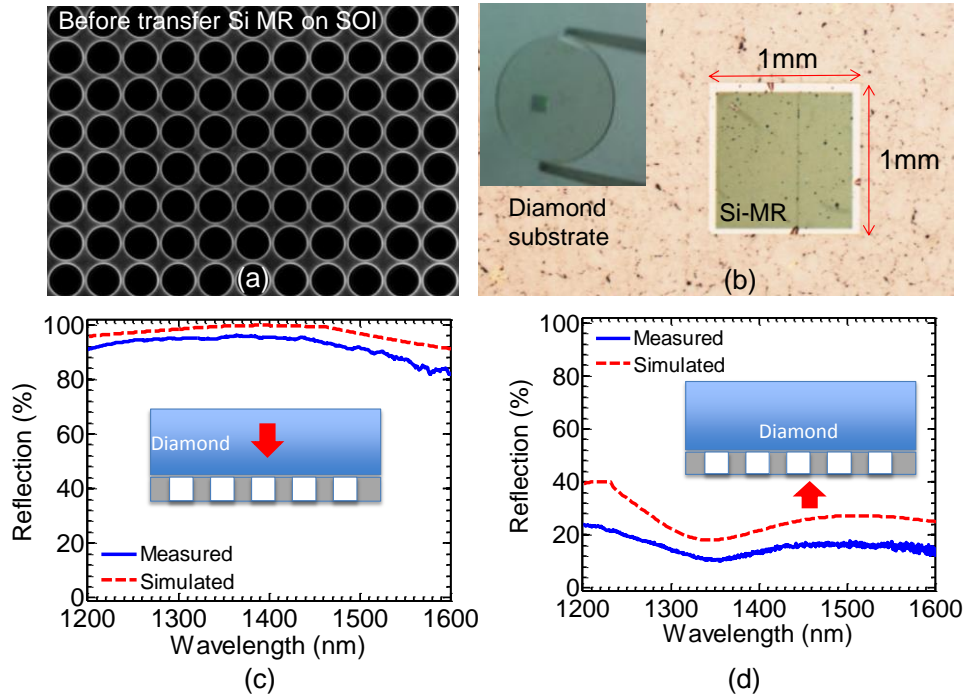


**Fig. 16** (a) SEM of Si-MR sitting on SOI; (b) Image of transferred Si MR on diamond substrate, inset is the whole pictures of the sample; (c) and (d) Reflections of Si-MR on diamond with incidence from the substrate and top side.

the Si-MR on SOI and the photo image the Si MR on diamond substrate. The quality of the transferred Si-MR is pretty good. The surface black dot comes from the diamond surface itself, which can be seen outside Si MR region in Fig. 16 (b). The both reflections from substrate and the top Si side are measured and shown in Fig. 16(c) and (d) with simulated reflections together (note here  $R=1-T$  is used for the incidence from substrate to avoid the diamond surface reflection in normalization). We can see the measured and simulated reflection match well. And the



reflection from the substrate is as high as expected and can be improved by improving transfer quality and using more smooth diamond substrate.

To confirm the good thermal performance of Si MR on diamond, considering the broad band reflection spectra shift is not obvious with small temperature change, we prepared two Si membrane high Q filters transferred on glass and diamond substrates to compare the peak or dip shift with incident power or temperature. Fig. 17 (a) and (b) show the images of the transferred high Q filters on glass and diamond substrate, respectively. We use high power green laser (spot diameter around 3-4mm) to heat the high Q filters (area  $\sim 1\text{mm} \times 1\text{mm}$ ). The sketch of the testing condition is shown in Fig. 17 (c). As increasing heating power, the reflection peak of the filter on glass shifts around 2.5nm to longer wavelength as shown in Fig. 17(d), while the reflection dip of the filter on diamond does not shift shown in Fig. 17(e). It is the evidence the diamond with good thermal conductivity is much help to heat dissipation. So, the Si MR on diamond is a better reflector candidate for high power VCSEL.

Fig. 18(a) shows another new MR-VCSEL cavity design using diamond as MR and heat spreader simultaneously. The blue curve in Fig. 18(b) shows the simulated reflection

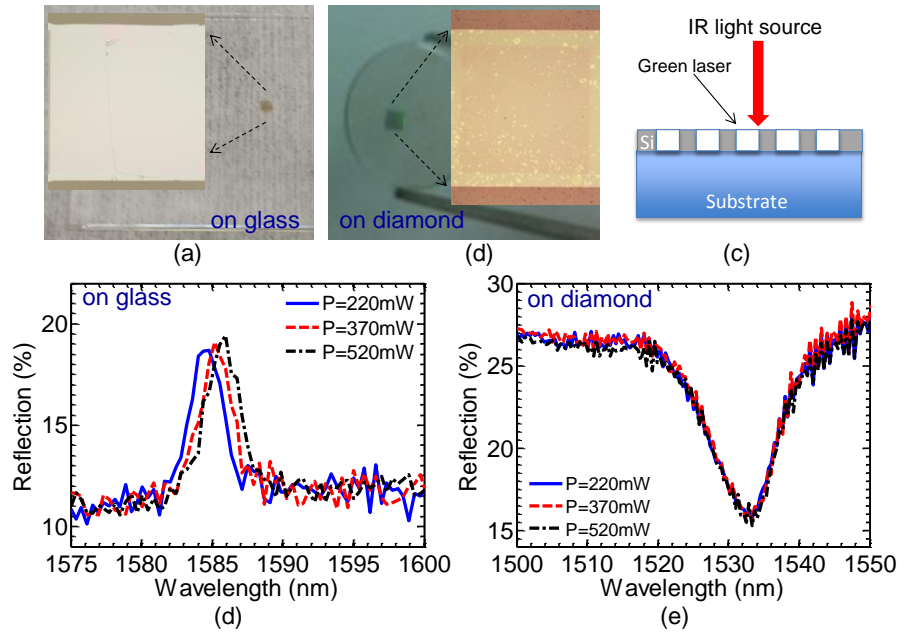


**Fig. 17** (a) and (b) Images of Si membrane high Q filters on glass and diamond substrates; (c) sketch of the reflection test with green laser heating; (d) and (e) reflections of the two filters vs green laser heating power.

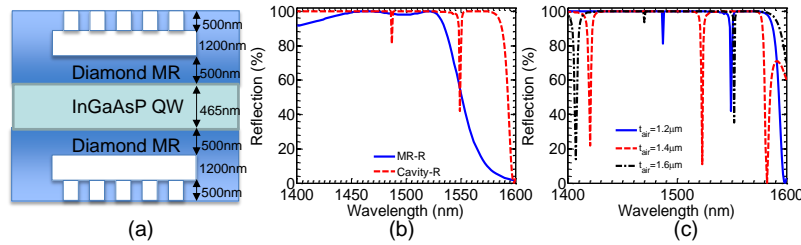


**Fig. 18** Sketch of MR-VCSEL design with diamond as MR and heat spreader; (b) Reflections of diamond-MR (blue solid line) and cavity (dashed red line) with the structure parameter shown in (a); (c) Reflection for cavity with different air gap thickness.

performance of the diamond MR with PC pattern (thickness=0.5 $\mu\text{m}$ ,  $a=1.1\mu\text{m}$ ,  $r=0.42a$ ). Its high reflection (>99%) band covers from 1450 – 1530nm with center wavelength of 1500nm. As shown in Fig. 18 (b), the cavity mode (dashed red line) of 1490nm is designed close to the reflection band center with the cavity structure parameter shown in Fig. 18 (a). Tuning the thickness of the air gap or the diamond beside QW can get the different cavity resonant mode location, as shown in Fig. 18(c). Note, the air gap can't be reduced to less than 1 $\mu\text{m}$  to keep the high reflection performance of diamond-MR.

Since diamond has a higher refractive index than glass, it is not suitable directly to be used as a Si-MR substrate. To get a Si-MR on diamond substrate, we propose a novel design although it is a little complicated, as shown in Fig. 19(a). The diamond surface needs to be periodically or randomly patterned with much smaller air hole (less than half of Si-MR PC lattice) to reduce the effective index. The air hole depth should be larger than 1 $\mu\text{m}$ . Fig. 19(b) shows three designs with different air hole size in diamond substrate. The designed reflection band with  $R>98\%$  covers from 1480 -1600nm with center wavelength around 1530nm.

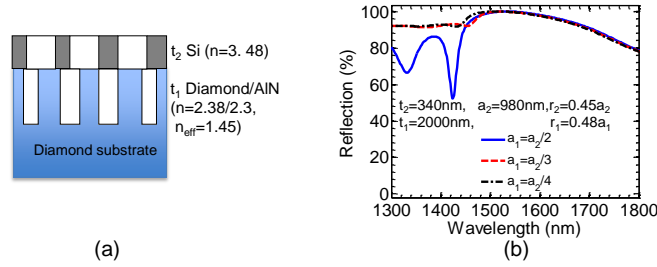


**Fig. 19** Sketch of Si-MR sitting on surface patterned diamond substrate; (b) Reflections of Si-MR with three kinds of diamond PC pattern on its surface, the structure parameters are listed in above figures.